TRIBHUVAN UNIVERSITY

INSTITUTE OF ENGINEERING

PULCHOWK CAMPUS

THESIS NO: M-107-MSESPM-2015/2019

Analytical Modeling and Performance Evaluation of Gravitational Water Vortex Runner

by

Nipesh Regmi

A THESIS

SUBMITTED TO THE DEPARTMENT OF MECHANICAL ENGINEERING

IN PARTIAL FULFILLMENT OF THE REQUIREMENTS FOR THE

DEGREE OF MASTER OF SCIENCE IN

ENERGY SYSTEM PLANNING AND MANAGEMENT

DEPARTMENT OF MECHANICAL ENGINEERING

LALITPUR, NEPAL

NOVEMBER, 2019

COPYRIGHT

TRIBHUVAN UNIVERSITY

INSTITUTE OF ENGINEERING

PULCHOWK CAMPUS

DEPARTMENT OF MECHANICAL ENGINEERING

The undersigned certify that they have read, and recommended to the Institute of Engineering for acceptance, a thesis entitled **"Analytical Modeling and Performance Evaluation of Gravitational Water Vortex Runner"** submitted by Nipesh Regmi in partial fulfilment of the requirements for the degree of Master of Science in Energy System Planning and Management.

Supervisor, Dr. Shree Raj Shakya

Associate Professor

Department of Mechanical Engineering

External Examiner, Prof. Hari Prasad Neopane, PhD

Department of Mechanical Engineering

Kathmandu University

Committee Chairperson, Dr. Nawraj Bhattarai

Head

Department of Mechanical Engineering

Date

ABSTRACT

Gravitational Water Vortex Power Plant (GWVPP) needs optimization either in its structure or runner for enhancing power extraction from low pressure head. The study is focused on Computational Fluid Dynamics (CFD) analysis of basin followed by design and analysis of the runner for GWVPP using multiphase analysis. The tapered ratios of the basin were varied with and without changing exit hole and corresponding variations in flow parameters were observed.

The design of the runner is based on the methodology that maximum energy can be extracted when the flow strikes the runner perpendicularly. The methodology was applied for obtainining runner profile for basin structure of different tapered ratios. The CFD analysis as well as experimental validation of runner designed for reference basin were carried out. Bronze material was used for the fabrication of the runner for experimental analysis. The maximum efficiency of designed runner was found to 7.93% at 68 rpm from computational analysis while experimentally it was found to be 12.10% at 66 rpm. However, comparison at the same runner speed of 66 rpm, the experimental maximum efficiency was found to be higher by 4.45% than computational efficiency 7.65%.

ACKNOWLEDGEMENT

Foremost, I would like to express the deepest appreciation to my supervisor, Dr. Shree Raj Shakya, Assistant Professor, Department of Mechanical Engineering, Pulchowk Campus, for being side by side, providing immense support and supervison for my thesis. Without his guidance and persistent help this thesis would not have been possible.

I would like to express my sincere gratitude to Hari Dura, Assistant Professor, Department of Mechanical Engineering, Pulchowk Campus for continuous support of my thesis and research for his patience, motivation, enthusiasm, immense knowledge and for providing me with access to computer workstations. His guidance helped me in all the time of research and writing of thesis. I could not have imagined having a better advisor and mentor for my thesis.

I am grateful to Sudip Bhattarai, Assistant Professor, Department of Mechanical Engineering, Pulchowk Campus for enlightening me the first glance of research on this topic. I thank to Himalaya College of Engineering, Chyasal, Lalitpur for allowing me to carry out experimental works with conical basin setup that supports my thesis. My sincere thanks also goes to Er. Ankit Gautam and Er. Raj Kumar KC for helping me during experiment. Thanks to Center for Energy Studies (CES), Pulchowk Campus and Baburaja Maharjan, Deputy Manager, Nepal Electricity Authority for providing me with the instrumentations.

I thank to Zener Technologies, Kupondole, Kathmandu for 3D printing; Tuladhar Metal Works, Bijeshwori, Kathmandu for helping with the casting process; Shrestha Lathe Milling Workshop, Sinamangal, Kathmandu for machining works; Shumsher and Chhotu Auto Workshop, Bhotebahal, Kathmandu for helping with gas welding.

I thank my mate Er. Rama Sapkota and Ramesh Shrestha, Assistant Manager, Nepal Electricity Authority for the stimulating discussions, for academic supports and for working together before deadlines. Also I thank my friends Er. Suman Acharya, Er. Shubhash Joshi and Er. Milan Adhikari for their support.

Finally, I would like to acknowledge with gratitude, the support and love of my family- my parents, Naranath and Sushila; my brother, Nikash; my sisters, Nisha and Nipesha. They all kept me going.

TABLE OF CONTENTS

LIST OF TABLES

LIST OF FIGURES

LIST OF SYMBOLS

L_C	:	Canal length
A_H	:	Air- domain height
u	:	Velocity component along X-axis
v	:	Velocity component along Y-axis
w	:	Velocity component along Z-axis
V	:	Resultant velocity vector

LIST OF ABBREVIATIONS

ANSYS	:	ANalysis SYStems
CATIA	:	Computer Aided Three-Dimensional Interactive Application
CFD	:	Computational Fluid Dynamics
GWVPP	:	Gravitational Water Vortex Power Plant
MATLAB	:	MATrix LABoratory

CHAPTER-ONE: INTRODUCTION

1.1. Background

Electricity supply in the rural areas of Nepal remains as one of the most challenging issues due to the high infrastructure cost and losses, lack of road, and poor returns compounded by constrained government budgets resulting from the geographical profile of Nepal (Banerjee, et al., 2011). So, there is a need for most cost-efficient off-grid renewable energy system for enhancing the rural electrification.

The hydropower plants with higher water pressure are economically feasible whereas mini and micro hydro power plant (100-1000 kW) with lower water pressure (0.70 m up to 2.00 m) is not economical with conventional turbines (Rahman, et al., 2016). The Francis and the Reaction turbines are not suitable when the hydraulic head is lower than 2 m (Jost, et al., 2014). The Kaplan and the Pelton turbines can be scaled down for smaller hydro power plant but typically limited to hydraulic heads greater than 3m (Abbasi & Abbasi, 2011). Hence, an alternate option to harvest energy from low head water resources is essential.

Gravitational Water Vortex Power Plant (GWVPP), under the category of micro-hydro scheme, has been considered as one of the technology for harvesting electricity from low hydraulic head (0.7 m to 2 m) using the energy available in the vortex flow (Zotloeterer.com, 2011). For the very first time, the technology was invented by Austrian Engineer, Franz Zotlöterer while he was looking for an efficient way to aerate the water in 2007 (Wanchat & Suntivarakorn, 2011; Dhakal, et al., 2015). In GWVPP, water is channelled through a large, straight inlet, and then passes tangentially into a round basin, forming a powerful vortex (whirlpool). The basin has a hole at the center bottom that acts as an outlet. A vertical axis turbine is placed at the centre of the vortex which withdraws rotational energy from gravitational vortex. The turbine does not work on pressure differential but on the dynamic force of the vortex. This type of power generation system is suitable in areas where low velocity water flows such as small rivers and existing agricultural irrigation canals are available.

1.2. Problem Statement

The development of Gravitational Water Vortex Power Plant system was started few years back. It is a not well-developed technology for power extraction from low pressure water energy sources. Basin optimization had been very popular amongst the researchers following its development to achieve maximum power output. Limited literatures are available on the design, fabrication and physical geometry of the vortex turbine and generator (Rahman, et al., 2017).

The past study had found that the parameters including turbines, inlet height and flow rates have significant effects on the efficiency of vortex power plant. Turbine, being most important component of GWVPP system needs to be optimized for maximizing power output (Dhakal, et al., 2015; Marius-Gheorghe, et al., 2013). Need for optimization of profile of the turbine blade is recommended by the study of Rahman, et al. (2017). Achieving an efficient design for runner requires appropriate understanding of the flow behaviour that are actually taking place in the system.

Experimental and more often hit and trial method are widely used for designing runner profile. Some latest studies however tried in designing runner profile via understanding of the flow pattern inside basin. But their studies assumed basin top surface as wall during CFD analysis. These assumptions limit the analysis of basin in their studies as a completely closed channel analysis thereby deviating from actual conditions. As basin top is open to atmosphere, it is therefore necessary to analyse the basin with top surface open such that an interaction with atmosphere can be taken into consideration.

This study focused on designing of the runner for GWVPP system, by CFD analysis of the basin ensuring that the top surface of basin is open to atmosphere and resembles to actual conditions.

1.3. Objectives

1.3.1. Main Objective

The main objective of this study is to develop an analytical method based on CFD analysis for designing gravitational water vortex runner and evaluate its performance.

1.3.2. Specific Objectives

The main objective will be accomplished with the following auxiliary objectives:

i. To model and carry out CFD analysis to study the flow pattern for available GWVPP basin.
ii. To develop analytical method for designing blade profile based on CFD analysis results.
iii. To evaluate the performance of the designed runner.

1.4. Assumptions and Limitations

1.4.1. Assumptions

i. Maximum energy will be extracted when the flow strikes the runner perpendicularly.

1.4.2. Limitations

i. Unstructured mesh has been used for CFD Analysis.
ii. No advance corrections on points obtained for runner profile.

1.5. Scope of Works

The scope of the study can be stated as follow

i. The method can be used for preliminary design of GWVPP runner for a given basin with the flow velocity and runner position from basin top surface provided.
ii. The methodology can be used as reference for preliminary design of other types of turbine.

CHAPTER-TWO: LITERATURE REVIEW

2.1. Gravitational Water Vortex Power Plant

For the very first time, this plant was constructed by Austrian Engineer, Franz Zotlöterer that operates on a low-head as little as 0.7 meters and utilizes the inherent kinetic energy of artificially induced vortex. The water passes through a large, straight inlet, and then passes tangentially into a round basin, forming a powerful vortex, which finds its outlet at the center bottom of the shallow basin. The construction cost for such plant is half that of a conventional hydroelectric installation of similar yield with positive impact on environment (Zotlöterer, 2016).

Several advantages of this plant are listed below (Lepisto, 2007).

i. At the discharge of the vortex, contaminants are evenly distributed through the water, which is also oxygenated, leading to improved efficiency of natural micro-organisms to decompose the contaminates: hence, cleaner water downstream.

ii. The increased contact area between the water and air results in better cooling evaporation during the warm season, and a perimeter of ice insulates the water in the cold season- all the while the turbine continues gently turning out the Watts.

iii. The temperature self-regulation capacity of the water is further enhanced by the concentration of the densest water at the middle of the vortex. Since water is densest at 4°C, water which is warmer than 4°C tends to be cooled when it is pulled into the vortex and cooler water is warmed by the mixing which the vortex causes. Biodiversity downstream is enhanced by the stabler temperatures.

2.2. Vortex Flow

A flow where all the streamlines are concentric circles about a given point (Anderson, 2001). There are mainly two types of vortex flow, namely forced vortex flow and free vortex flow as explained:

A. Forced Vortex Flow

In a forced vortex flow, the fluid mass is made to rotate by means of some external power source, which exerts a constant torque on the fluid mass. This torque induces the whole mass of fluid to rotate at constant angular velocity. A most common example of a forced vortex flow is the motion of a vertical cylinder containing liquid rotated about its central axis with a constant angular velocity.

B. Free Vortex Flow

In a free vortex flow, no external torque is required to rotate the fluid mass. The motion may be due to the rotation imparted previously to the fluid particles or due to some internal action (i.e., fluid pressure itself or the gravity force). Most common examples of vortex flow are flow of liquid through basin sink, whirlpool in river, etc.

2.3. Computational Fluid Dynamics

Computational fluid dynamics is the science of predicting fluid flow, heat transfer, mass transfer, chemical reactions, and related phenomena by solving the mathematical equations which govern these processes using a numerical process.

2.3.1. Working of CFD (Bakker, 2008)

- Analysis begins with a mathematical model of a physical problem.
- Conservation of mass, momentum and energy must be satisfied throughout the region of interest.
- Fluid properties are modeled emperically.

- Simplifying assumptions are made in order to make the problem tractable (e.g., steady-state, incompressible, inviscid, two-dimensional).
- Provide appropriate initial and boundary conditions for the problem.
- CFD applies numerical methods (called discretization) to develop approximations of the governing equations of fluid mechanics in the fluid region of interest.
- The solution is post-processed to extract quantities of interest (e.g. lift, drag, torque, heat transfer, separation, pressure loss, etc.).

Discretization refers to the division of domain into a finite set of control volumes or cells. The discretized domain is called the "grid" or the "mesh". General conservation (transport) equations for mass, momentum, energy, etc., are discretized into algebraic equations and all equations are solved to render flow field.

2.3.2. Elements of CFD (Tu, et al., 2018)

CFD code consists mainly of following three modules

A. Preprocessing

This is the first step of CFD simulation process which helps in describing the geometry in the best possible manner. One needs to identify the fluid domain of interest. The domain of interest is then further divided into smaller segments known as mesh generation step. There are different popular Pre-Processing software available in the market including: Gridgen, CFD-GEOM, ANSYS Meshing, ANSYS ICEM CFD, TGrid etc. The steps are summarized as:

i. Creation of Geometry
ii. Mesh Generation
iii. Selection of Physics and Fluid Properties
iv. Specification of Boundary Conditions

B. Solver

Once the problem physics has been identified, fluid material properties, flow physics model, and boundary conditions are set to solve using a computer. There are popular commercial software available for this including: ANSYS FLUENT, ANSYS CFX, Star CCM, CFD++, OpenFOAM etc. All these software have their unique capabilities. Using this software; it is possible to solve the governing equations related to flow physics problem. The steps are summarized as:

i. Initialization
ii. Solution Control
iii. Monitoring Solution
iv. Monitoring Convergence

C. Postprocessing

The next step after getting the results is to analyze the results with different methods like contour plots, vector plot, streamlines, data curve etc. for appropriate graphical representations and report. Some of the popular post-processing software include: ANSYS CFD-Post, EnSight, FieldView, ParaView, Tecplot 360 etc. The following results can be obtained:

i. X-Y graphs
ii. Contour
iii. Velocity Vectors
iv. Data Report and Output
v. Animation

2.3.3. Turbulence Model

A turbulence model is a computational procedure to close the system of mean flow equations. These models allow the calculation of the mean flow without first calculating the full time-dependent flow field. Common turbulence models are

- Classical models based on Reynolds Averaged Navier-Stokes (RANS) equations (time averaged)

i. Zero equation model: mixing length model

ii. One equation model: Spalart-Allmaras

iii. Two equation mdoels: $k-\epsilon$ style models (Standard, RNG, Realizable), $k-\omega$ model, and ASM

iv. Seven equation model: Reynolds stress model

- Based on space-filtered equations

i. Large eddy simulation

RNG $k-\epsilon$ model

This model was derived from the application of a statistical technique called renormalization group theory. The model is similar in form to the standard $k-\epsilon$ model but the following refinements are included.

i. Additional term in ϵ equation for interaction between turbulence dissipation and mean shear.

ii. Effect of swirl on turbulence.

iii. Analytical formula for turbulent Prandtl number.

iv. Differential formula for effective viscosity.

The model has an improved predictions for high streamline curvature and strain rate, transitional flows and wall and heat and mass transfer. However, it still doesn't predict the spreading of a round jet correctly.

Transport Equations for RNG $k-\epsilon$ model

- Turbulent kinetic energy:

$$\frac{\partial}{\partial t}(\rho k)+\frac{\partial}{\partial x_i}(\rho k U_i) = \frac{\partial}{\partial x_j}\left(\alpha_k \mu_{eff}\frac{\partial k}{\partial x_j}\right)+G_k+G_b-\rho\epsilon-Y_M+S_k \quad \text{Equation 2.1}$$

- Dissipation rate:

$$\frac{\partial}{\partial t}(\rho \epsilon)+\frac{\partial}{\partial x_i}(\rho \epsilon U_i) = C_{1\epsilon}\left(\frac{\epsilon}{k}\right)(G_k+C_{3\epsilon}G_b)+\frac{\partial}{\partial x_j}\left(\alpha_\epsilon \mu_{eff}\frac{\partial \epsilon}{\partial x_j}\right) - C_{2\epsilon}\rho\left(\frac{\epsilon^2}{k}\right)-R_\epsilon+S_\epsilon \quad \text{Equation 2.2}$$

Where,

G_k	=	Generation of turbulence kinetic energy due to mean velocity gradient
G_b	=	Generation of turbulence kinetic energy due to byouancy
Y_M	=	Contribution of the fluctuating dilatation in compressible turbulence to the overall dissipation rate
$\alpha_k, \alpha_\epsilon$	=	Inverse effective Prandtl numbers for k and ϵ
S_k, S_ϵ	=	User-defined source terms

2.4. Related Works

Singh & Nestmann (2009) studied on the optimization of a free vortex propeller runner for micro hydro application where the head does not exceed 2 meters. The study focused on developing hydraulically optimized propeller turbines for the micro hydro range. The propeller turbine used have been designed using the free vortex theory operating in a gross head from 1.5 m to 2 m and discharge of approximately 75 l/s. Several modifications were carried out on the design for the purpose of improving the runner performance. The performance of the runer was very sensitive to changes in exit tip

angle. The optimized experimental runner delivered 810 watts of shaft power at 1.75 m and 900 rpm consuming 64 l/s of water with operating efficiency of 73.9%. The researchers suggested to study the feasibility of other design approaches like constant blade reaction and zero power blading designs. Also, the study lack the influence of the number of blades and hub to tip ratio on the runner performance.

MARIAN, et al. (2012) recommended for helical turbine steps with hydrofoil profile. The study further shows that, due to large variation along the peripheral velocity, there is a need for twisting blade.

Marius-Gheorghe, et al. (2013) found experimentally that maximum energy can be extracted when the runner is placed near the outlet and these results were validated with theories.

Dhakal, et al. (2014) performed an experiment and found that the conical basin has greater vortex strength than that of cylindrical basin. Greater efficiency was found at the bottommost position and agreed with the results of Gheroghe, et al. (2013). Smaller number of blades produces greater efficiency while increment in blade radius decreases the efficiency of turbine. The maximum efficiency recorded was 25.36%.

Dhakal, et al. (2015) performed an experiment and found that the optimal position of turbine is 65% to 75% of GWVPP's height and verified that the conical basin has higher overall power output with a maximum efficiency of 36.84%.

Power, et al. (2016) performed an experiment and found that efficiency was found to increase with increase in number of blades. This finding however goes against the results of Dhakal, et al. (2014). This indicate that there might be an optimal number of blades for turbine. The maximum efficiency of the vortex power plant was found to be 15.1%.

Rahman, et al. (2016) designed and tested a model free vortex power generation system under different water pressure and turbine parameters at Material and Mineral Research Unit Laboratories, Faculty of Engineering, University Malaysia Sabah. The study concluded that the tangential velocity at the vortex free surface was highest for 0.12 m water head and maximum efficiency of about 43% was achieved with three blades and 0.027 m turbine outer diameter. Also, the study found that in case of vortex power generation system the maximum hydraulic efficiency was recorded when the turbine

rotating speed was half of the vortex tangential velocity. A very week relation is observed between turbine speed and hydraulic efficiency.

Sapkota, et al. (2016) study on the runner of the GWVPP with conical basin to improve its efficiency. The study takes into consideration of different runner parameters like impact angle, inlet and outlet blade angle, number of blades, taper angle of blades, surface area of blades, blade profile etc. The study was carried out with the assumption that only impulse action of the water is responsible for the rotation of the turbine. 20 different runners have been developed computationally and tested experimentally. The impact angle, inlet and outlet blade angles, number of blades, tapered angle for conical profiles were optimized. A linear relationship of power output with flow rate were formulated both computationally and experimentally.

Wichian & Suntivarakorn (2016) studied the effects of turbine baffle plates on the efficiency of water free vortex turbines. The CFD program was used to design baffle plates with diameter of 45 cm and height of 32 cm. The results showed that 5 baffle plates, with a propeller baffle area of 50%, gave the highest degree of torque. The turbines, which had been installed with 50% baffle plates, had shown an increase in torque and average efficiency of 10.25% and 4.12% respectively concluding the fact that baffle plates can help to increase efficiency.

A study of Dhakal, et al. (2016) focused on the optimization of the runner to improve the efficiency of the GWVPP. CFD analysis was carried out on three different design of runner with straight, twisted and curved blade profile. The ANSYS CFX was used to analyze the fluid flow through the channel, basin, turbine hub and blade whose results were used for evaluating the efficiency of each runner. The study found that the curved blade profile have higher efficiency with peak efficiency 82.4% compared to 46.31% for the straight blade runner and 63.54% for twisted blade profile. Experimental analysis showed the peak efficiency point of 71.01% at 0.5 m head for curved profile runner. The assumptions for the study was similar to that of Sapkota, et al. (2016) i.e., only the impulse action of flow is considered.

A review paper of Rahman, et al. (2017) presented with the past literatures related to GWVPP suggested that there is a need for optimized shape and blade profile to achieve maximum efficiency.

CHAPTER-THREE: RESEARCH METHODOLOGY

This chapter presents an insight on how the research was carried out.

3.1. Research Framework

The study was carried out by following the framework as shown in Figure 3.1.

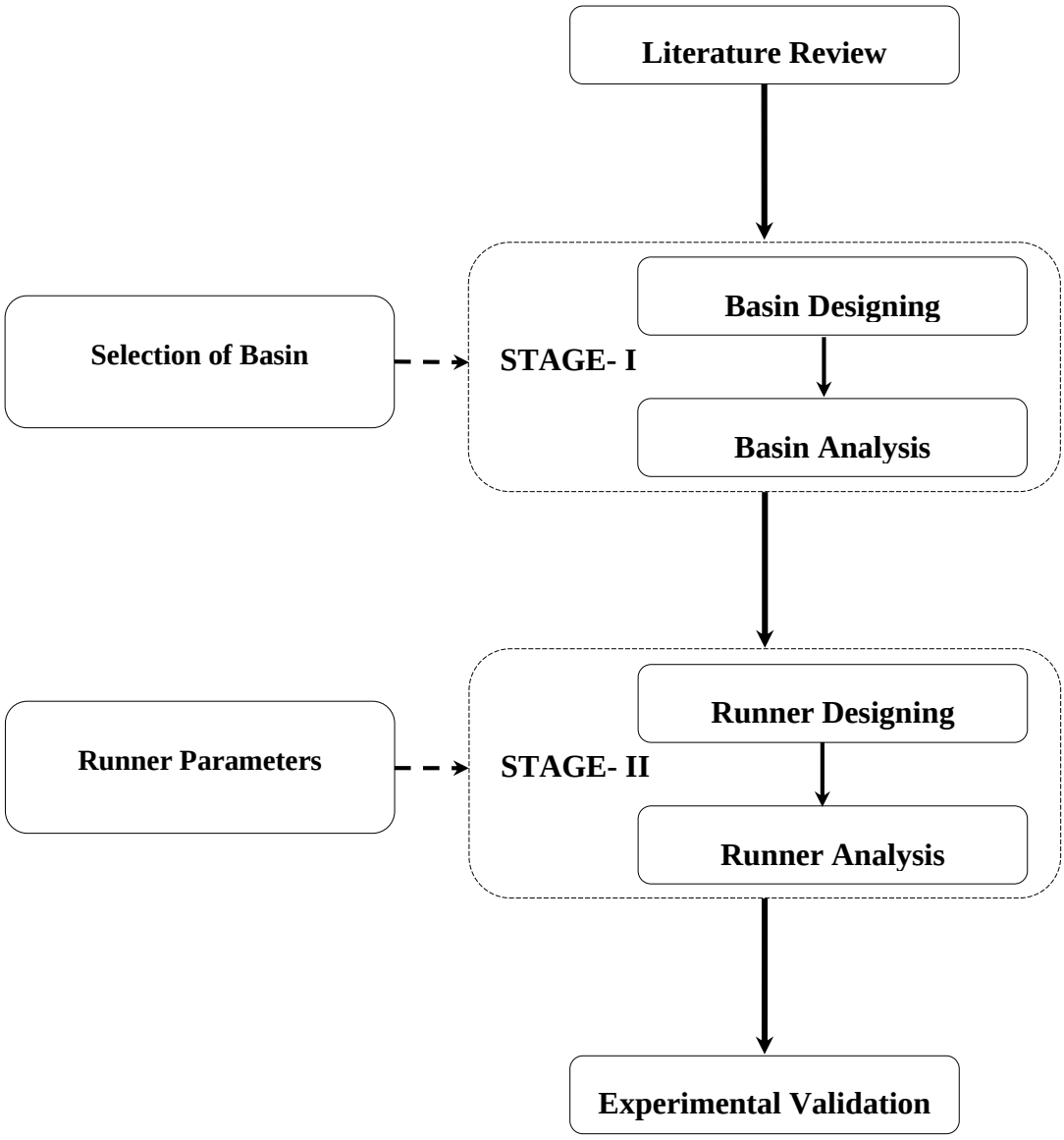

Figure 3.1 Research methodology chart

The methodology has been divided into two major stages viz. Design & analysis of basin and Design & analysis of runner followed by experimental validation of the runner designed for selected reference basin.

3.2. Basin Design and Analysis

The methodology adopted for the CFD analysis of Basin is shown in Figure 3.2.

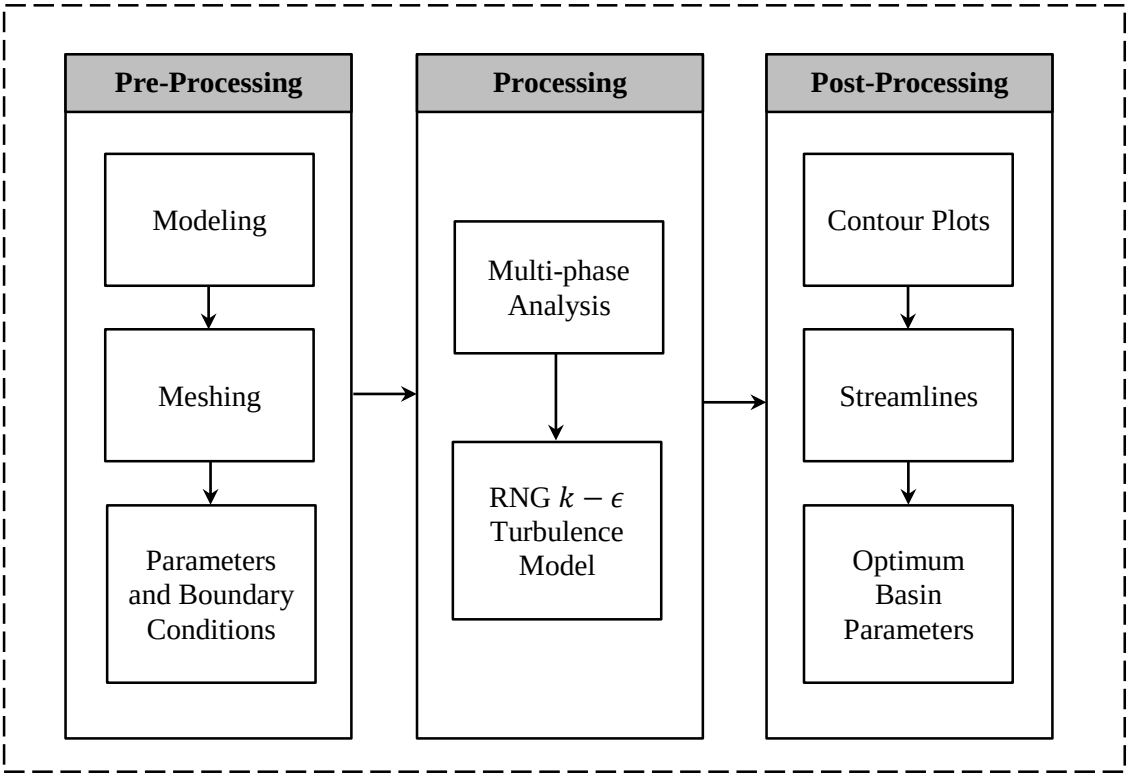

Figure 3.2 Methodology for CFD analysis of basin

During this stage, the reference basin was selected for study. Different geometrical studies were carried out on basin so as to obtain more appropriate geometry for modeling in further study. The appropriate boundary conditions were assigned to the geometry and was analysed using multiphase approach using RNG $k-\epsilon$ turbulence model. The velocity contours and streamlines were then observed for design of runner.

3.2.1. Basin Designing

3.2.1.1. Design Requirement of Basin

As suggested by the study of Dhakal, et al. (2014) and Dhakal, et al. (2015), the conical basin was selected for the study. The schematic drawing with major dimensions of reference basin is shown in Figure 3.3. Since, this basin test rig was available in the campus premises, and therefore be used for testing of runner for experimental validation in the latter part of the thesis work.

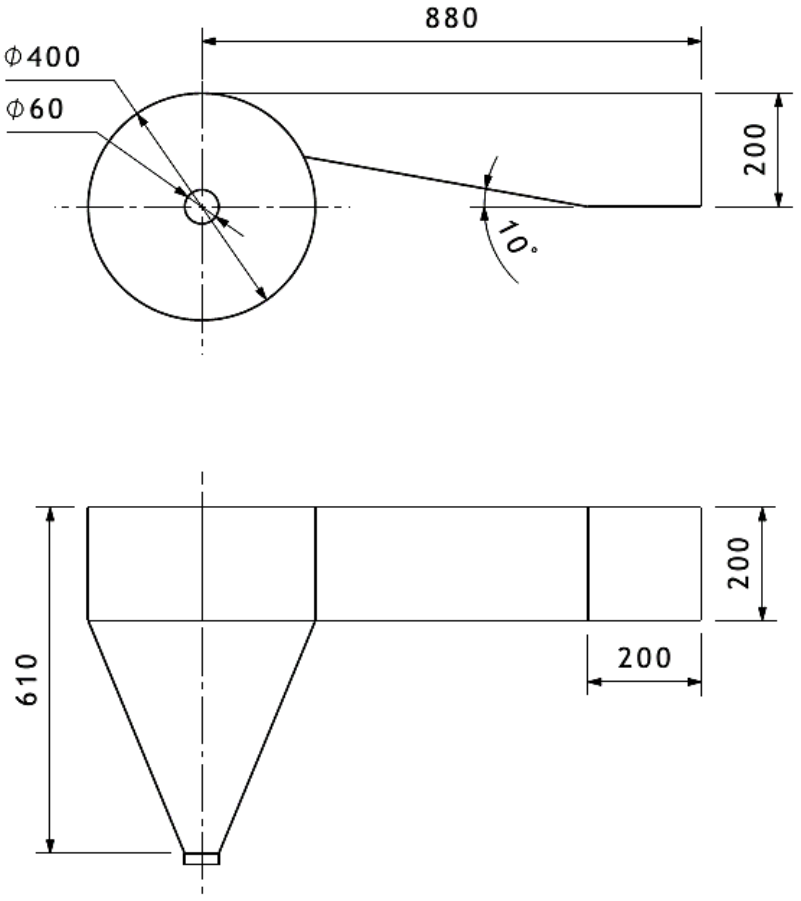

Figure 3.3 Schematic drawing of reference basin with major dimensions

3.2.2. Modelling of the Basin

The basin was modeled in CATIA V5R20 which is then imported to ANSYS CFX Design Modeler as a solid model. The basin was finalized after having detailed study on several parameters of basin such as air-admission height, canal length, etc.

3.2.3. Basin Mesh

Automatic Mesh were generated for the study in ANSYS CFX. Tetrahedral elements were used for meshing. The meshed basin for final study is as shown in Figure 3.4 and major mesh details are presented in Table 3.1.

Table 3.1 Mesh Details used in Final Model

Particulars	**Remarks**
Sizing	
Size Function	Proximity and Curvature
Relevance Center	Fine
Transition	Slow
Span Angle Center - Curvature Normal Angle - Num Cells Across Gap	Fine - Default (18.0°) - Default (3)
Proximity Size Function Sources - Min Size - Proximity Min Size - Max Face Size - Max Tet Size - Growth Rate	Faces and Edges - Default (2.4467e-004 m) - Default (2.4467e-004 m) - Default (2.4467e-002 m) - Default (4.8934e-002 m) - Default (1.20)
Automatic Mesh Based Defeaturing - Defeature Size	On - Default (1.2233e-004 m)
Minimum Edge Length	0.18850 m
Quality	
Check Mesh Quality - Target Skewness	Yes, Errors - Default (0.900000)
Smoothing	Medium
Mesh Metric - Min - Max - Average - Standard Deviation	Orthogonal Quality - 1.7307e-002 - 0.99667 - 0.79051 - 0.11397
Statistics	
Nodes	175943
Elements	989562

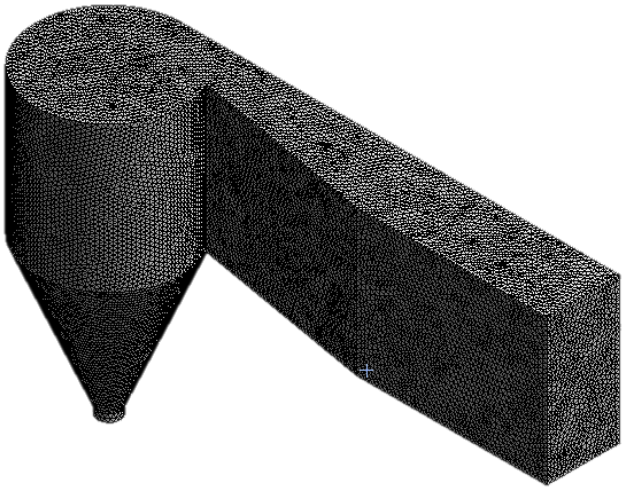

Figure 3.4 Basin mesh used for final study

Because of the complexity of basin geometry, unstructured mesh has been used, as more time is required for the generation of structured meshes.

3.2.3.1. Mesh Independence Study

Prior to performing final CFD simulations for a problem, it is necessary to carry out mesh independent study to make sure that the solution is independent of the mesh resolutions. This allow us to reduce the mesh size without losing accuracy and, therefore, reducing the computational effort.

The mesh independence study was performed by taking the RNG k-ϵ model with the scalable wall function with the inlet velocity of 0.25 m/s for reference basin selected initially. Seven meshes of different sizes with the number of elements varying from 112954 to 1039630 were used for mesh independence study. Torque acting on the wall of conical basin was observed as a key parameter of interest. In the present work the convergence criteria of 10^{-4} was used. The graph was plotted between number of elements and torque as shown in Figure 3.5.

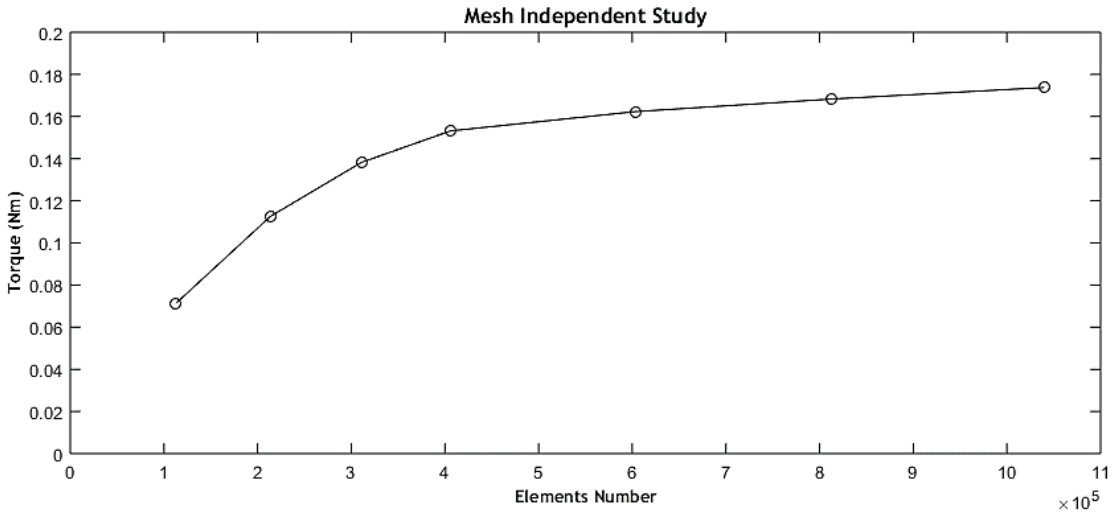

Figure 3.5 Mesh independent study for basin

As can be seen in figure, when the number of elements was higher than 813080, the torque on the conical basin wall became nearly unchanged and remained within 3.15% of value than when the elements number was 1039630. Hence total 813080 was used for all subsequent computations with average mesh density of 6798700 elements per cubic meter of geometry volume.

3.2.4. Effect of Canal Length and Air-Domain Height on Reference Basin

The reference basin being open to atmosphere at top surface, it was indeed necessary to consider the atmospheric effect upon the flow inside the basin. Also, for considering the fully developed flow, it is necessary to study how canal length affect the flow. The effect of increasing the canal length, L_C and adding air domain height, A_H were studied. The parameters canal length and air-domain height for study are presented in Figure 3.6.

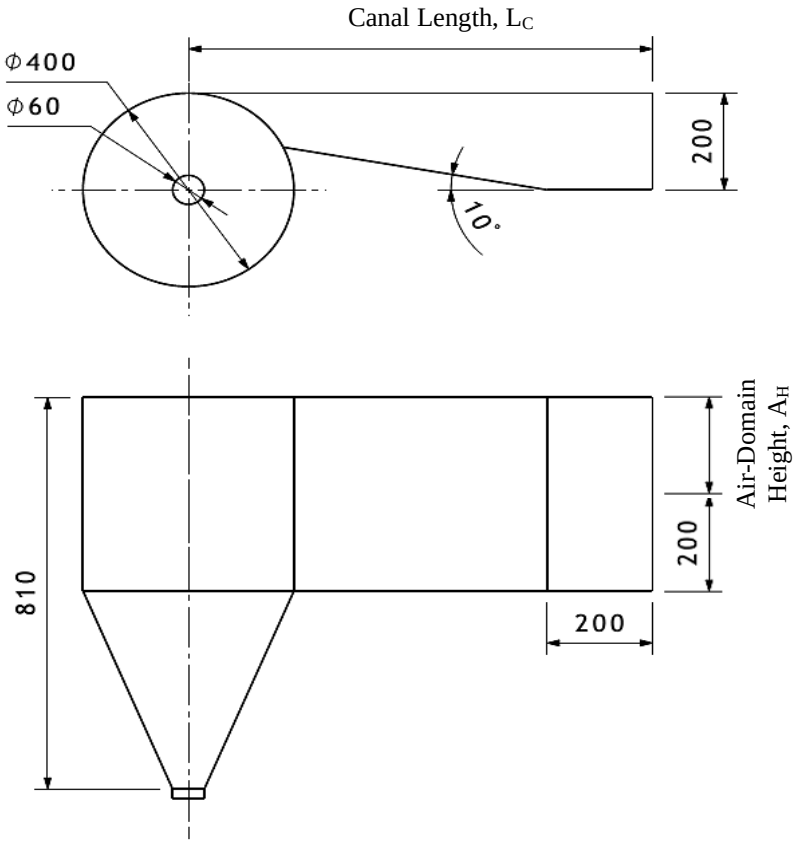

Figure 3.6 Reference basin with parameters considered for study

3.2.4.1. Canal Length Independent Study

Five different simulations were carried out by varying the length of canal in the range from 880 mm to 3000 mm. The torque acting on the conical basin wall was considered as key parameters of interest during these study. The physics setup was similar to that of mesh independent study. The mesh density was used in proportion for longer canal length as obtained from mesh indpendent study. The graph was plotted between canal length and the torque as shown in Figure 3.7.

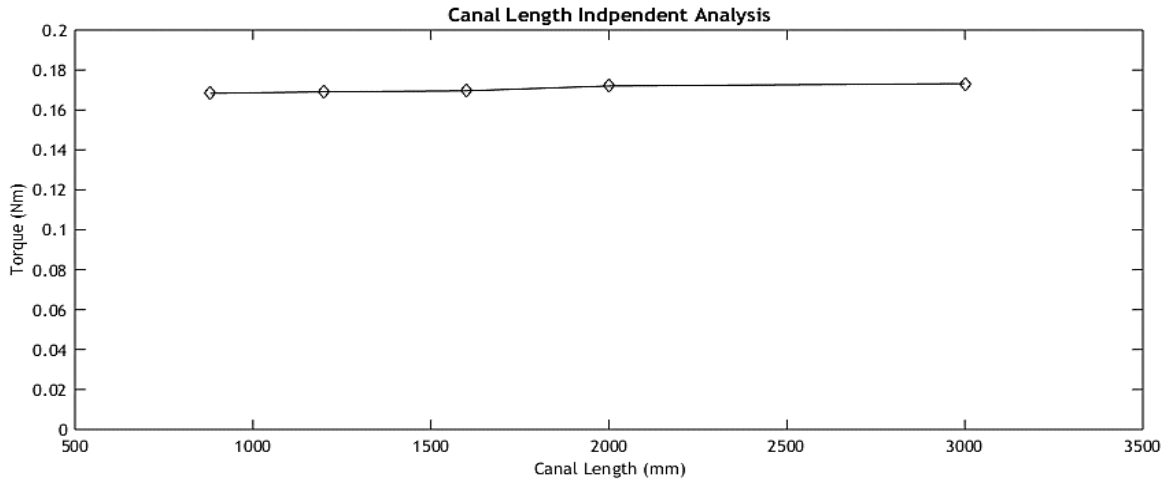

Figure 3.7 Canal length independent study for basin

The figure shows that, increasing the length of canal basin has not significant effect on the torque developed. So for the entire study, the canal length was chosen to 1200 mm as no much change was observed in the torque.

3.2.4.2. Air Domain Height Independent Study

The inlet canal height for the basin were varied keeping water portion height constant at 200 mm. Here again, the mesh density was used in proportion for increasing air-admission height as obtained from mesh indpendent study. The air portion heights were increased from 0 mm to 400 mm and then corresponding torque developed on the conical portion of basin were observed. The graph was plotted between air domain height and the torque as shown in Figure 3.8.

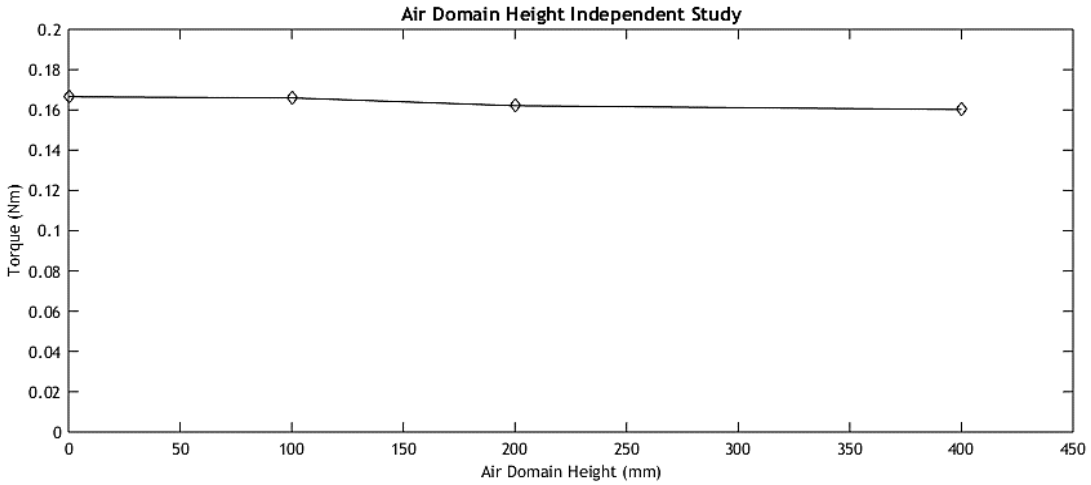

Figure 3.8 Air domain height independent study for basin

From the figure, it was observed that changes in developed torque when the air domain heights were 200 mm and 400 mm were almost constant. Hence, air domain height of 200 mm was considered for this study to observe the flow behavior of flowing water in air region. With this detail, the basin for final modeling was determined. The schematic of final basin model with major dimensions to be used for further analysis is shown in Figure 3.9.

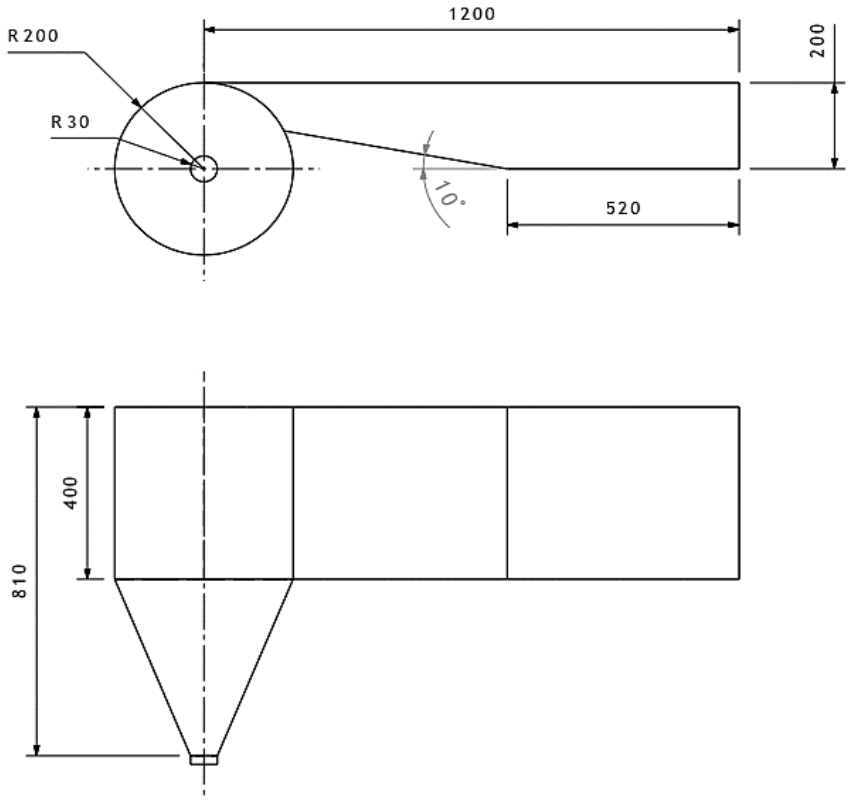

Figure 3.9 Final basin model with major dimensions

3.2.5. Basin Analysis

The analysis is based on multiphase Eulerian fluid approach where two fluids, air and water, occupy same domain. The temperature of the domain is set to $25°C$ and the reference pressure is set to 1 atm. The buoyancy reference density is set to the density of air at $25°C$ which is equal to 1.2 kg/m^3.

3.2.5.1. Governing Equations

The continuity equation and Navier Stokes equations for a steady incompressible, viscous and turbulent flow (density $\rho =$ constant, viscosity $\mu =$ constant), with a velocity field $\vec{V} = (u_r, u_\theta, u_z)$ are

Continuity Equation

$$\frac{1}{r}\frac{\partial(ru_r)}{\partial r} + \frac{1}{r}\frac{\partial u_\theta}{\partial \theta} + \frac{\partial u_z}{\partial z} = 0 \qquad \text{Equation 3.1}$$

Navier Stokes Equation

Radial-Direction

$$\begin{aligned} u_r\frac{\partial u_r}{\partial r} + \frac{u_\theta}{r}\frac{\partial u_r}{\partial \theta} - \frac{u_\theta^2}{r} + u_z\frac{\partial u_r}{\partial z} \\ = -\frac{1}{\rho}\frac{\partial p}{\partial r} \\ + \frac{\mu}{\rho}\left\{-\frac{u_r}{r^2} + \frac{1}{r}\frac{\partial}{\partial r}\left(r\frac{\partial u_r}{\partial r}\right) + \frac{1}{r^2}\frac{\partial^2 u_r}{\partial \theta^2} + \frac{\partial^2 u_r}{\partial z^2} - \frac{2}{r^2}\frac{\partial u_\theta}{\partial \theta}\right\} + g_r \end{aligned} \qquad \text{Equation 3.2}$$

Transverse-Direction

$$\begin{aligned} u_r\frac{\partial u_\theta}{\partial r} + \frac{u_\theta}{r}\frac{\partial u_\theta}{\partial \theta} + \frac{u_r u_\theta}{r} + u_z\frac{\partial u_\theta}{\partial z} \\ = -\frac{1}{\rho}\frac{\partial p}{\partial \theta} \\ + \frac{\mu}{\rho}\left\{-\frac{u_\theta}{r^2} + \frac{1}{r}\frac{\partial}{\partial r}\left(r\frac{\partial u_\theta}{\partial r}\right) + \frac{1}{r^2}\frac{\partial^2 u_\theta}{\partial \theta^2} + \frac{\partial^2 u_\theta}{\partial z^2} - \frac{2}{r^2}\frac{\partial u_r}{\partial \theta}\right\} + g_\theta \end{aligned} \qquad \text{Equation 3.3}$$

Axial-Direction

$$\frac{\partial u_z}{\partial t} + u_r\frac{\partial u_z}{\partial r} + \frac{u_\theta}{r}\frac{\partial u_z}{\partial \theta} + u_z\frac{\partial u_z}{\partial z} = -\frac{1}{\rho}\frac{\partial p}{\partial z} + \frac{\mu}{\rho}\left\{\frac{1}{r}\frac{\partial}{\partial r}\left(r\frac{\partial u_z}{\partial r}\right) + \frac{1}{r^2}\frac{\partial^2 u_z}{\partial \theta^2} + \frac{\partial^2 u_z}{\partial z^2}\right\} + g_z \quad \text{Equation 3.4}$$

Solving the equations analytically is almost impossible due to complexity of equations. And due to this reason, ANSYS CFX was used for the solution of these equations.

3.2.6. Simulation Parameters for Basin Analysis

The two fluids viz. air and water are defined for analyis of the basin. The built-in fluid models are used for both fluids. The properties of water and air are taken at $25°C$ and 1 atm pressure. In the production of air-core vortices, the buoyancy plays a vital role, therefore, buoyancy is also included in the analysis.

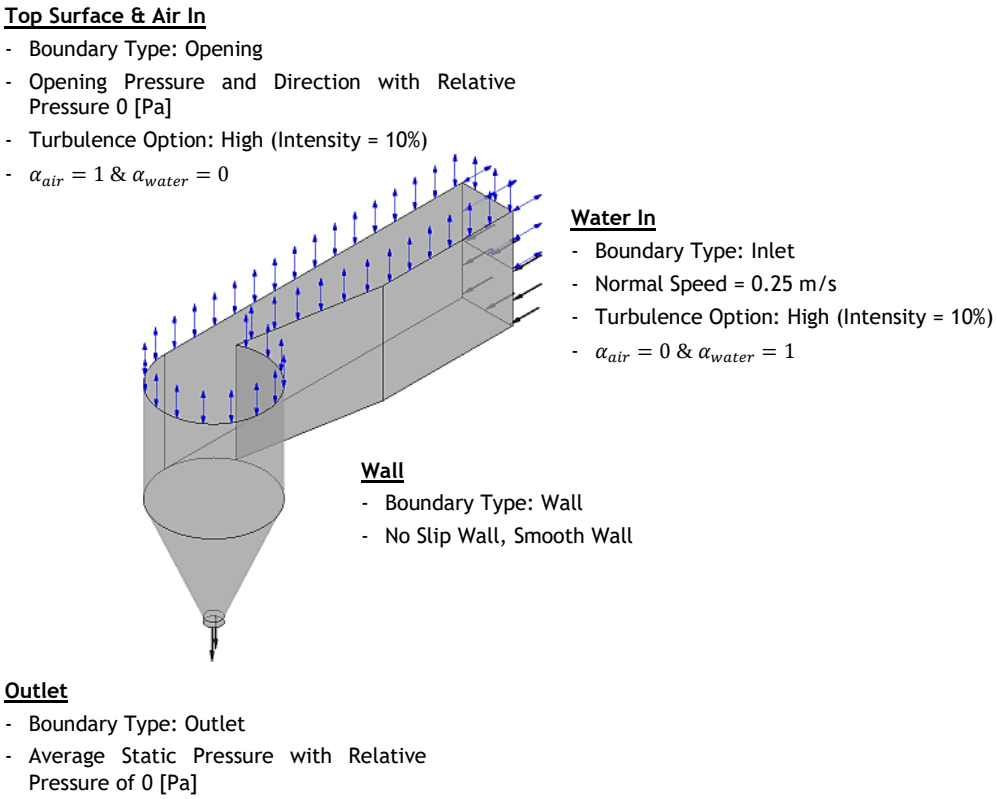

Figure 3.10 Boundary conditions for basin analysis

Turbulence model used was RNG $k-\epsilon$ (Dhakal, et al., 2015). Also the comparative study of WU, et al. (2012) between RNG $k-\epsilon$ Turbulence model and Standard $k-\epsilon$ Turbulence model concluded that RNG $k-\epsilon$ Turbulence model is more suitable for

the simulation of air core vortices as compared to Standard $k-\epsilon$ Turbulence model due to great curving streamline flows. Due to the presence of both air and water in the basin, multiphase domain was defined for the analysis. The boundary conditions used for the basin analysis are defined as shown in Figure 3.10.

Here, α_{air} defines the volume fraction of air while α_{water} defines the volume fraction of water. The walls of the basin were set as smooth walls.

3.2.6.1. Solver Parameters

The model include advection scheme as "High Resolution" and turbulence numeric was "High Resolution". Timescale was set to "Physical Timescale". The number of iterations was set to 100000 with a residual target of 0.0001.

3.3. Runner Design and Analysis

The methodology adopted for CFD analysis of Runner is shown in Figure 3.11.

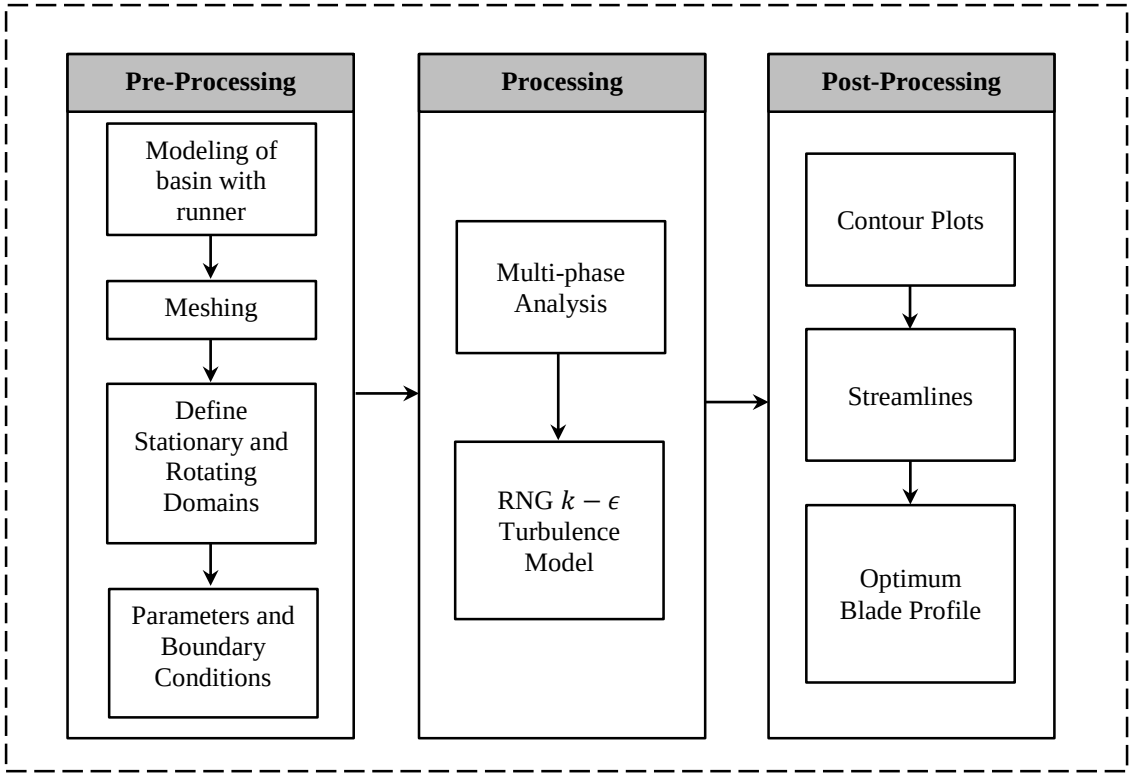

Figure 3.11 Methodology for CFD analysis of runner

3.3.1. Runner Blade Designing

The velocity contour plots and streamlines obtained from CFD analysis of the basin were used as input for designing of runner blades. The design of blades were based on the assumptions that the maximum energy is extracted when water strikes the runner perpendicularly.

Some of the parameters that were assumed during the design of runner blades are presented in Table 3.2.

Table 3.2 Assumed Data for Runner Blade Design

Particulars	Value (mm)	Remarks
Depth of runner top edge from top surface of water level in basin	200.00	
Height of runner	210.00	
Clearances for runner blades on either side (hub & shroud side)	20.00	10% of top radius of basin used

Designing of the runner blades can be explained in the following steps:

A. Selection of Planes and Points

A YZ-plane was considered for design and nine different points lying on the plane were selected in the domain as shown in Figure 3.12.

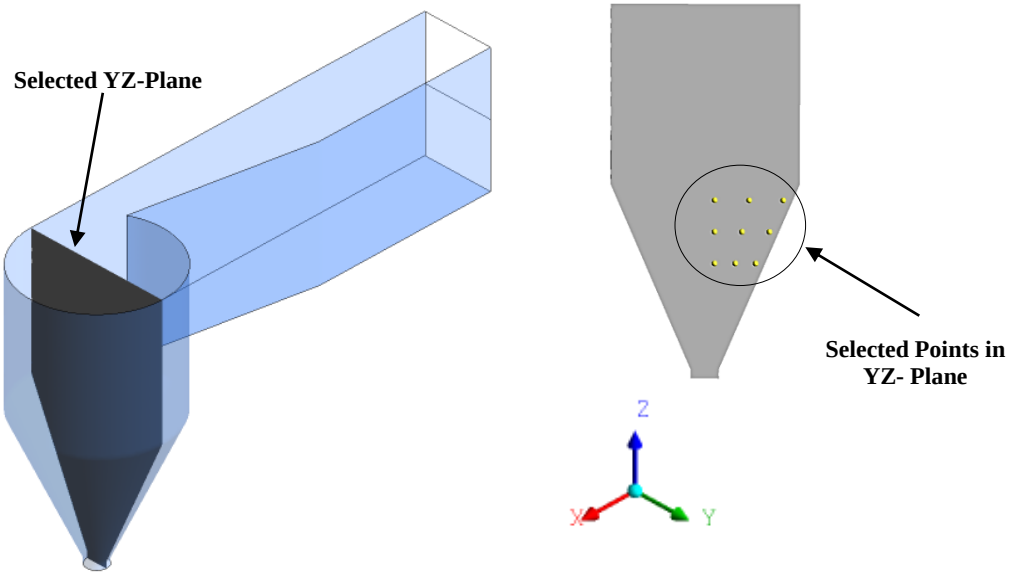

Figure 3.12 Plane and points selected for design of blade

The nine different points were considered for simplicity and to reduce computations time for analytical calculations to obtain the final points that will be used in designing blade profile. The co-ordinates of points selected on the YZ- plane are presented in Table 3.3.

Table 3.3 Co-ordinates of Runner Analysis Points (mm)

Point	x	y	z	Point	x	y	z	Point	x	y	z
1	0.00	20.00	-235.00	2	0.00	92.75	-235.00	3	0.00	165.49	-235.00
4	0.00	20.00	-305.00	5	0.00	78.23	-305.00	6	0.00	136.46	-305.00
7	0.00	20.00	-375.00	8	0.00	63.72	-375.00	9	0.00	107.44	-375.00

These were the major points used for design of the blade profile. However, for every points considered above, two different points above and below the considered points at height and depth of one-sixth times the total runner height were taken and represented them as T and B point.

For example, the two different points above and below point 1 were named as 1T and 1B respectively. All these points 1T, 1 and 1B lies on the same vertical line.

B. Velocity Components at Considered Points

The velocity components at each considered points were then determined from CFD analysis of the basin and are listed in Table 3.4.

Table 3.4 Velocity Components at Considered Points

Point	Position (m)			Velocity (m/s)			
	x	y	z	u	v	w	V
1	0.000	0.020	-0.235	-0.303507	0.200569	-0.155828	0.395761
2	0.000	0.093	-0.235	-1.09828	0.0671452	-0.223127	1.12273
3	0.000	0.165	-0.235	-0.909101	0.0840538	0.109156	0.919481
4	0.000	0.020	-0.305	-0.426647	0.283744	-0.279207	0.583519
5	0.000	0.078	-0.305	-1.07506	0.0923348	-0.229751	1.10321
6	0.000	0.136	-0.305	-1.02981	0.0678781	0.0487325	1.03319
7	0.000	0.020	-0.375	-0.598034	0.22194	-0.475928	0.795871
8	0.000	0.064	-0.375	-1.09351	0.0878861	-0.346512	1.15046
9	0.000	0.107	-0.375	-1.10959	0.0413845	-0.073848	1.11282

C. Blade Profile in Side Plane

The YZ plane was considered as a front plane and XZ plane was considered as a side plane during design. Designing in XZ plane required the y-component of velocity to

disappear. Taking x-component and z-component of velocities, angle made by velocity vector with positive z-axis were determined and are presented in Table 3.5.

Table 3.5 Angle Made by Velocity Vectors with Positive Z-Axis

Point	Velocity Component (m/s)			Angle with positive z-axis (Degree)
	u	v	w	
1	-0.303507	0	-0.155828	114.55
2	-1.09828	0	-0.223127	101.26
3	-0.909101	0	0.109156	83.2
4	-0.426647	0	-0.279207	118.7
5	-1.07506	0	-0.229751	101.8
6	-1.02981	0	0.0487325	87.29
7	-0.598034	0	-0.475928	121.91
8	-1.09351	0	-0.346512	106.81
9	-1.10959	0	-0.073848	93.8

Once, angle made by velocity vector at points considered were determined with positive z-axis, a line passing through the considered points and perpendicular to velocity vectors were determined. These obtained lines were then used for designing of blade profile in side plane. The process are illustrated as shown in Figure 3.13.

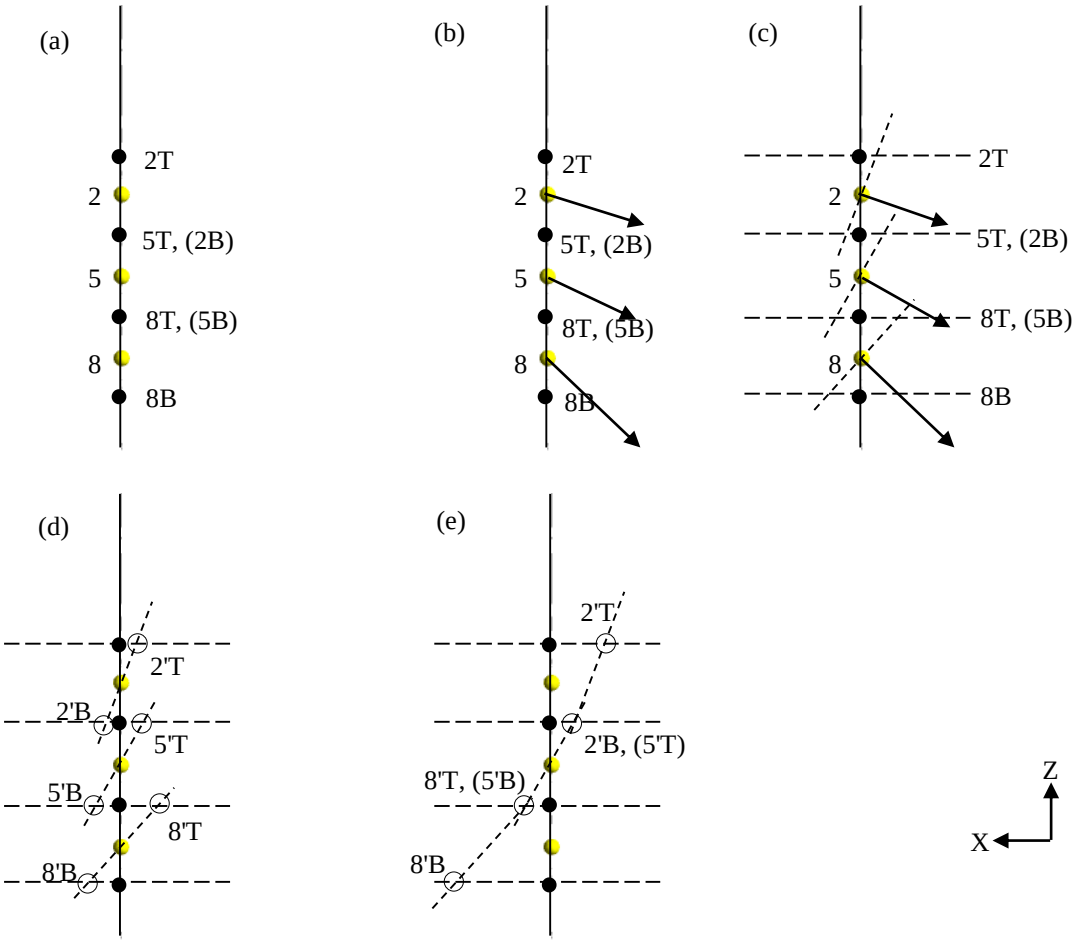

Figure 3.13 Illustration of blade profile design in side plane

Illustration for obtaining blade profile in side plane:

Figure 3.13 (a)

For illustration of obtaining blade profile in side plane, let us consider the major points 2, 5 and 8 along with their top and bottom points i.e. 2T and 2B for 2, 5T and 5B for 5 and 8T and 8B for 8.

Figure 3.13 (b)

The velocity vectors are then drawn for each major points.

Figure 3.13 (c)

The straight lines as represented by longer dotted lines parallel to x-axis are drawn passing from points 2T, 5T(2B), 8T(5B), 8B. The straight lines perpendicular to velocity vectors and passing through major points 2, 5 and 8 are also drawn as represented by short dotted lines.

Figure 3.13 (d)

The two different lines: one type-parallel to x axis passing througth top and bottom points of major points and second type passing through major points and perpendicular to velocity vectors intersect each other at new points named 2'T, 2'B, 5'T, 5'B, 8'T and 8'B.

Figure 3.13 (e)

The new obtained points are now shifted such that 5'T and 5'B remains as original points obtained in Figure 3.13 (d) while 2'B is made to coincide with 5'T and without changing the slope of line joining 2'B and 2'T, the new position of 2'T is obtained. The final points that are obtained in this figure are used for obtaining blade profile in side plane.

Similar method has been applied for other set of points viz. 1, 4 & 7 and 3, 6 & 9.

D. Correction of Points in Front Plane

However, while carrying out these process in side plane, there is some changes in front plane as well. So, there is need for correction of these points shift in front plane as well. The correction in front plane is carried out as shown in Figure 3.14.

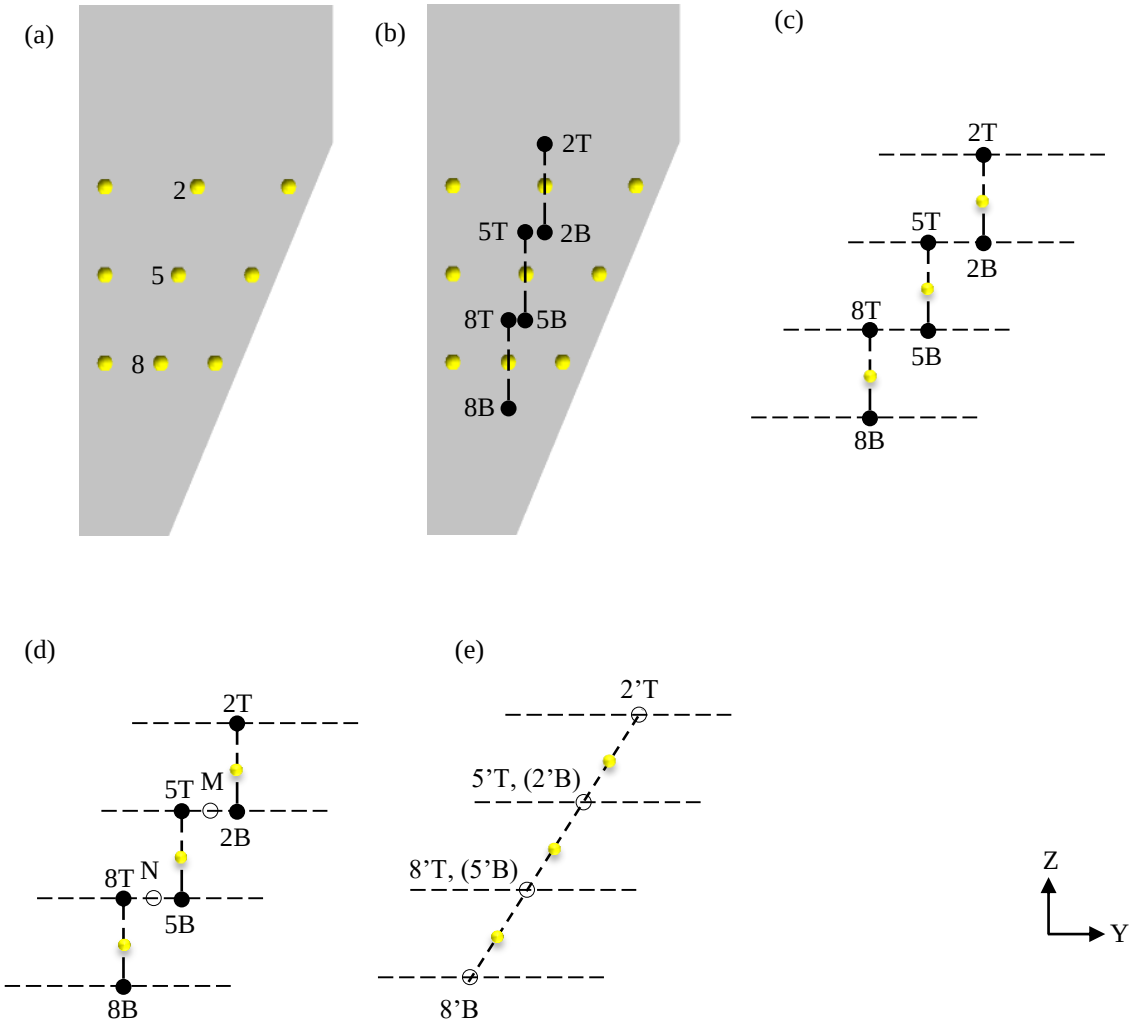

Figure 3.14 Correction of points in front plane

Illustration of correction of points in front plane:

Figure 3.14 (a)

For illustration of obtaining blade profile in side plane, let us consider the major points 2, 5 and 8.

Figure 3.14 (b)

The top and bottom points of corresponding major points i.e. 2T and 2B for 2, 5T and 5B for 5 and 8T and 8B for 8 are taken.

Figure 3.14 (c)

The straight lines as represented by longer dotted lines parallel to y-axis are drawn passing from points 2T, 5T(2B), 8T(5B), 8B.

Figure 3.14 (d)

For correcting the points in front plane, the mid-points joining 5T & 2B and 8T & 5B are determined as represented by M and N respectively. These mid points M & N are joined and extended to line drawn parallel to y-axis from point 2T and 8B to get new points 2'T and 8'B.

Figure 3.14 (e)

The points 2T is shifted to 2'T, 5T & 2B shifted to M (represented by 5'T & 2'B), 8T & 5B shifted to N (represented by 8'T & 5'B) and 8B shifted to 8'B. The final points that are obtained in this figure are the corrected points for generating blade profile.

Similar method has been applied for other set of points viz. 1, 4 & 7 and 3, 6 & 9.

Following the method as illustrated above, the points for generating blade profile in both side plane and front plane are obtained as presented in Table 3.6, Table 3.7 & Table 3.8.

Table 3.6 Final Co-ordinates to Plot for Major Points (1, 4 & 7)

Points for generating blade profile (1, 4 & 7)			
Points	**x**	**y**	**z**
1'T	-42.34	20.00	-200.00
1'B, 4'T	-15.02	20.00	-270.00
4'B, 7'T	15.02	20.00	-340.00
7'B	51.94	20.00	-410.00

Table 3.7 Final Co-ordinates to Plot for Major Points (2, 5 & 8)

Points for generating blade profile (2, 5 & 8)			
Points	**x**	**Y**	**z**
2'T	-20.86	100.00	-200.00
2'B, 5'T	-7.22	89.33	-270.00
5'B, 8'T	7.22	78.66	-340.00
8'B	27.12	67.99	-410.00

Table 3.8 Final Co-ordinates to Plot for Major Points (3, 6 & 9)

Points for generating blade profile (3, 6 & 9)			
Points	**x**	**y**	**z**
3'T	15.13	180.00	-200.00
3'B,6'T	3.44	158.66	-270.00
6'B,9'T	-3.44	137.32	-340.00
9'B	-4.36	115.98	-410.00

These points are now exported to CATIA V5R20 >> Shape >> Generative Shape Design and the generated blade profile is shown in Figure 3.15.

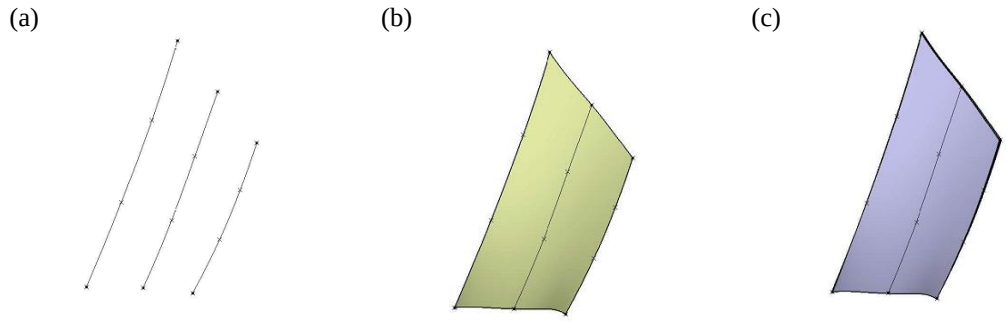

Figure 3.15 Blade profile generated using CATIA V5R20 (a) importing points to Generative Shape Design (b) surface using multi section surface (c) addition of thickness (2mm) to surface

3.3.2. Modelling of Runner

The designed runner blade obtained in Figure 3.15 is then used for achieving runner profile for GWVPP. Using the part design of CATIA V5R20, the final runner is achieved by arranging three blades each at an angle of 120°. For arrangement of blades, circular array feature is used. The hub used has an outer diameter of 40 mm and inner diameter of 20 mm. The final runner profile is shown in Figure 3.16.

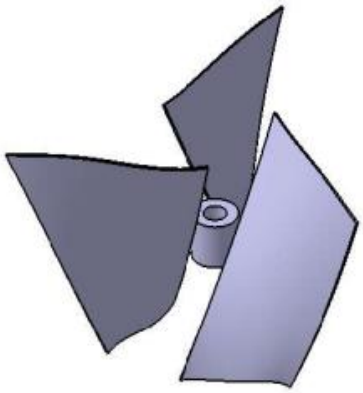

Figure 3.16 Designed runner for GWVPP

For enabling rotation of the blades in the basin, the basin was divided into two domains. An outer stationary domain, named as basin domain and a conical rotating domain containing the blades, named as runner domain as shown in Figure 3.17.

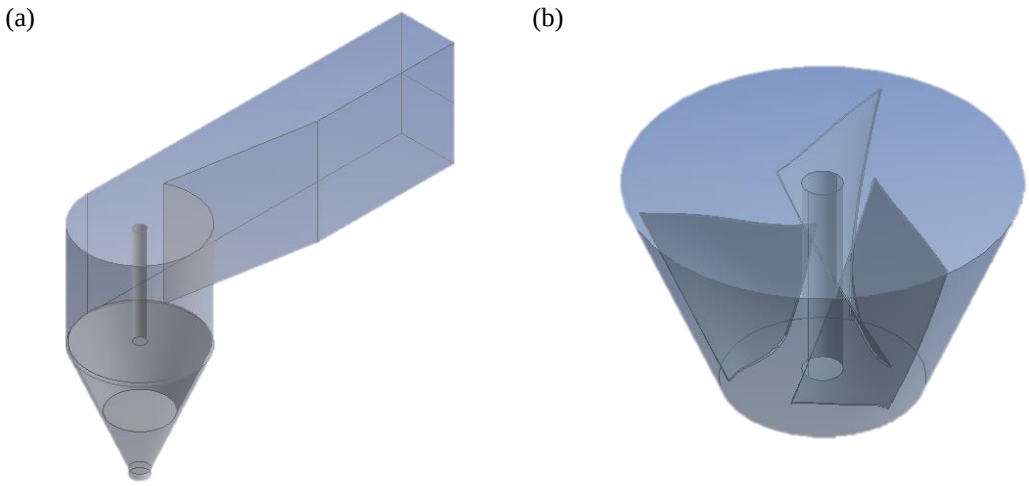

Figure 3.17 Domains (a) basin domain (stationary) (b) runner domain (rotating)

Runner domain enables the symmetric rotation of the blades without effecting stationary position of the basin domain. The runner domain and basin domain was imported to ANSYS CFX. The assembly of the basin domain and the runner domain is shown in Figure 3.18.

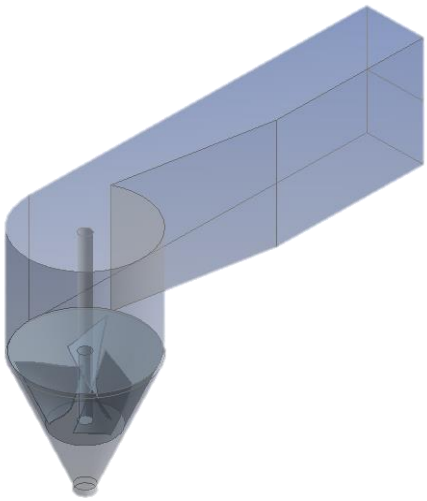

Figure 3.18 Basin domain and runner domain assembly

3.3.3. Runner Mesh

Automatic mesh was generated in ANSYS CFX Mesh using tetrahedral mesh elements. Body sizing was used for finer mesh. The meshing of the runner domain is shown in Figure 3.19.

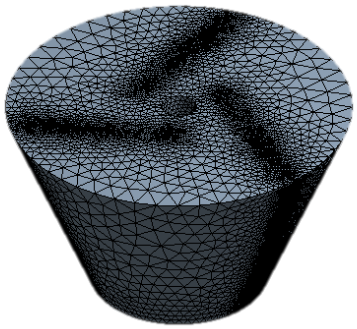

Figure 3.19 Runner domain meshing

The number of elements used for runner domain is 2046698 with the element size of 0.01085 m.

3.3.4. Runner Analysis

The analysis will be similar to basin analysis and will based on multiphase Eulerian fluid approach where two fluids, air and water, occupy same domain. The temperature of the domain will be set to $25°C$ and the reference pressure set to 1 atm. The buoyancy reference density will be set to the density of air at $25°C$ which is equal to 1.2 kg/m^3.

3.3.5. Simulation Parameters for Runner Analysis

In case of basin analysis, there is no blade domain, so the boundary conditions used are only those of the basin domain. Two fluids viz. air and water will be defined for this analyis as well. The properties of these fluids will be taken at $25°C$ and 1 atm pressure. The buoyancy will also be included in the analysis. The similar turbulence model as that used for basin analysis i.e. RNG $k-\epsilon$ turbulence model will be used.

The basin domain will be fluid domain and it is the stationary domain. Since the runner are the rotating components in the assembly, therefore the runner domain will be the rotating fluid domain and its rotational speed would be an input parameter in the analysis. The water inlet velocity will be fixed at 0.25 m/s. The boundarys conditions for runner analysis is shown in Figure 3.20.

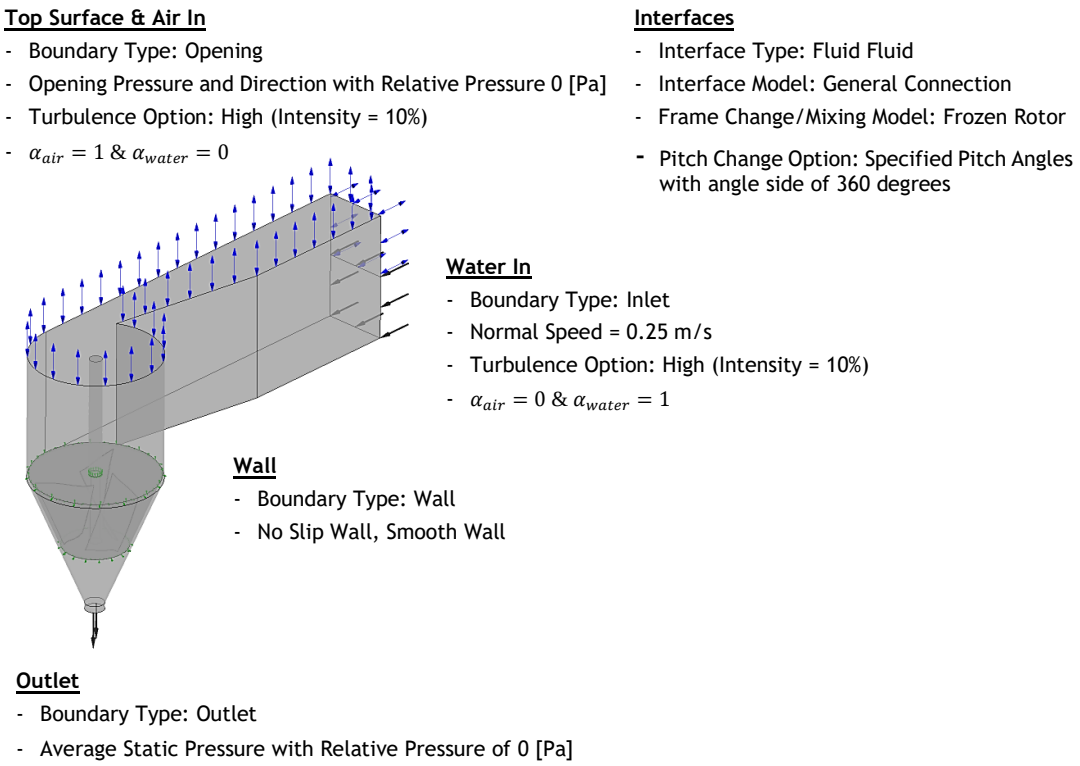

Figure 3.20 Boundary conditions for runner analysis

Here, α_{air} defines the volume fraction of air while α_{water} defines the volume fraction of water. The walls of the basin were set as smooth walls.

3.3.5.1. Solver Parameters

The model include advection scheme as "High Resolution" and turbulence numeric was "High Resolution". Timescale was set to "Physical Timescale". The number of iterations was set to 100000 with a residual target of 0.0001.

3.4. Experimental Setup

3.4.1. Test Rig

The laboratory scale down model as proposed by Dhakal, et al. (2014) available at Himalaya College of Engineering was used for testing of fabricated runner with the permission of Academic Director. The test rig used for experimental purpose is shown in Figure 3.21.

Figure 3.21 Test rig used for experiment

The test rig consisted of double chamber tank, canal, conical basin, submersible type pump for water delivery as major components. The dimensions and specifications of the major components of the test rig are shown in Table 3.9.

Table 3.9 Major Components of Test Rig with Dimensions

S.N.	Particulars	Specifications
1	Double chamber tank	Length × Width × Height: 1600 mm × 600 mm × 500 mm
2	90° V-notch	Notch Depth: 200 mm Notch Width: 400 mm Centrally Located
3	Submersible type centrifugal pump	Discharge: 9 litre/sec Head: 9000 mm Rpm: 10000
4	Water delivery pipe	Diameter: 80 mm Two 90° elbows
5	Drop chamber	Length × Width × Height: 200 mm × 400 mm × 650 mm
6	Gate valve	Diameter: 50 mm
7	Canal	Length × Width × Depth: 880 mm × 200 mm × 200 mm Notch Angle: 10°
8	Basin	Top Diameter: 400 mm Outlet Diameter: 60 mm Height: 610 mm
9	Shaft	Diameter: 20 mm Height: 650 mm
10	Bearing	Outer Diameter: 45 mm Inner Diameter: 20 mm
11	Supports	L-channel Iron Section (2 Nos.)

3.4.2. Instrumentations Used

(a) Torque Measurement

A rope brake drum type dynamometer was used for the measurement of torque. The jute rope was wounded round the pulley attached to the runner shaft and two digital spring balances were used at rope ends for measuring weight. The arrangement is as shown in Figure 3.22 (a). Same method has been adopted by Sapkota, et al. (2016) in

their study for torque measurement except that coconut rope was used instead of jute rope.

(b) Speed Measurement

The speed of the runner shaft was measured using testo 470 tachometer. The tachometer used is shown in Figure 3.22 (b). This tachometer has a measuring range from 1 to 99999 rpm with an accuracy of $\pm$ 0.02 % of measuring value.

(c) Flow Rate Measurement

The volumetric flow rate of the basin was measured with the aid of V-notch having included angle 90°.

(a)

(b)

Figure 3.22 (a) Torque measurement setup & (b) Tachometer

For experimental validation, the runner designed for reference basin with exit hole of diameter 60 mm was chosen.

3.4.3. Runner

3.4.3.1. Design Variations in Runner Parts for Fabrication

The actual profile of the runner blade were preserved during fabrication. However, the thickness has been changed from 2 mm to 6 mm to increase the blade strength. The height of the hub was taken to be the half of the total blade height i.e., 105 mm. The hub was fabricated with the outer diameter of 80 mm and inner diameter of 21 mm. The final design used for fabrication of hub and blade are shown in Figure 3.23.

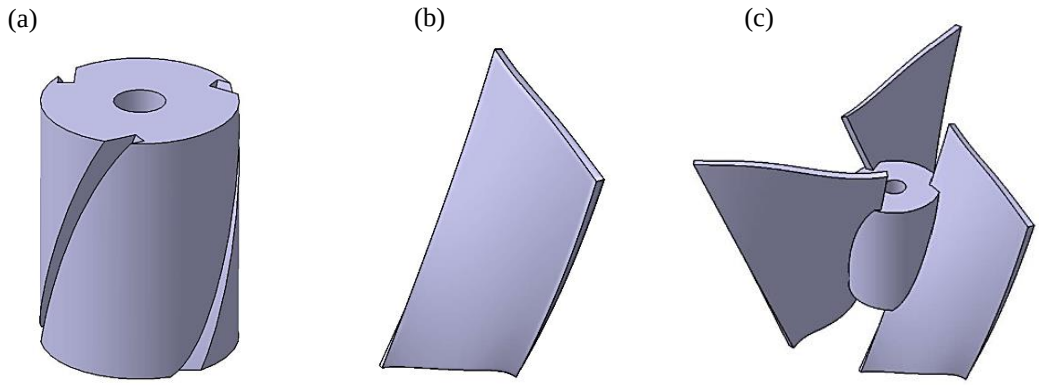

Figure 3.23 Final design for fabrication (a) hub (b) blade & (c) assembled hub and blades

Attachment of blades with hub

For attachment of blades with hub, the curved surface of the hub was provided with the slots that ran along the height of hub following blade profile as shown in Figure 3.23 (a). The blades had tight fit with the slots created in hub.

Attachment of runner hub with shaft

For attachment of hub with the shaft, three holes with thread were created at mid height of the hub. Three bolts (M6) were used through threaded hole to tighten the hub with shaft.

3.4.3.2. Fabrication of Runner Parts

Considering the limitation of time, the blade and hub of the runner were fabricated using 3D printing technology. Individual blades and hub were printed using ABS material. The fabricated runner blades and hub are shown in Figure 3.24.

(a)  (b) 

Figure 3.24 Fabricated runner parts (a) hub & (b) blade

3.4.3.3. Assembling of the Runner Parts

The printed blades and hub were then attached to form a complete runner as shown in Figure 3.25.

Figure 3.25 Assembled fabricated runner

The assembled runner was attached to the available shaft of the test rig at an appropriate position as shown in Figure 3.26 (a) and the attached runner along with the shaft is shown in Figure 3.26 (b).

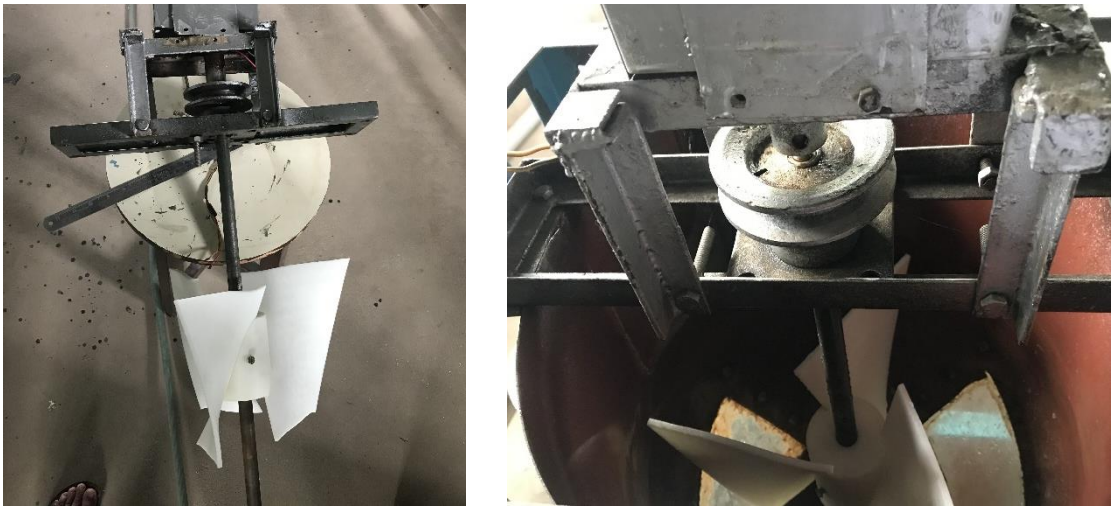

(a) (b)

Figure 3.26 (a) Attachment of fabricated runner in shaft (b) Placement of attached runner and shaft inside test rig basin

The experiment was unsuccessful with 3D printed runner. With the proceeding of the experiment, one of the runner blade broke down and was not able to take all necessary results. However, only one data was noted down with this runner before the blade broke down. The broken runner is shown in Figure 3.27.

Figure 3.27 Broken runner during experiment

Most probable reason behind breaking of the blade may be due to inappropriate infill used during the 3D print. The print was carried out with around 30% infill. The cross section of the broken blade is shown in Figure 3.28 which showed the weak infill of the material in the blade while printing.

Figure 3.28 Weak infill of the material during 3D print

The other reason may be due to inappropriate knowledge of material used in 3D printing technology. The ABS material was selected randomly without having prior knowledge and as per recommendations from previous study. Also, the inappropriate regulation of the flow through the canal and basin during the experiment and small thickness of the blade may be other possible causes of the damage of runner blade. Therefore, it is necessary to have proper knowledge on 3D printing setup, infill percent, printing materials and their strengths prior printing any product.

So, for verifying computational results, the runner was re-fabricated with the casting process using bronze material. The molds for blades and hub were made using same design as used for 3D printing. The blades and hub were casted differently as shown in Figure 3.29.

(a)

(b)

Figure 3.29 Fabricated using casting method (a) Hub & (b) Blades

The casted hub and blades were then attached using gas welding and the final runner obtained is as shown in Figure 3.30

Figure 3.30 Final casted runner after gas welding

This runner was then used for experimental validation. The fabricated runner was attached to the shaft available in the test rig via tightening of the bolt provided at the runner hub followed by placing the runner inside the basin at appropriate position as shown in Figure 3.31.

(a)

(b)

Figure 3.31 (a) Attachment of runner to shaft & (b) Placing the runner inside basin

Once the runner setup was done, the flow rate was then to be verified using notch formula as suggested by Pritchard (2010):

$$Q = 1.36\, H^{2.5}$$ Equation 3.5

The water level 'H' measured from tip of notch was maintained at 0.14 m so as to get the flow rate of 0.01 m^3/s. The water level in the notch was continuously observed to ensure that required flow is always obtained. The required experimental data were then observed from the experiment.

Figure 3.32 Experiment carrying out on casted runner

The costs involved in the entire process of fabrications and testing are summarized in Table 5.6 of ANNEX-3.

CHAPTER-FOUR: RESULTS AND DISCUSSION

4.1. Effect of Tapered Ratio on Flow Pattern and Runner Profile

The variations in the flow patterns and runner profile were obtained for two different cases. Initially, the tapered ratio of the conical basin were varied keeping the diameter of the exit hole constant and varying bottom cone diameter. Next, the tapered ratios of the conical basin were varied by changing the diameter of exit hole. Effect on flow pattern and runner profile due to each of the cases are explained.

4.1.1. Variation of Tapered Ratio with Constant Exit Hole

The diameter of the exit hole of the basin was kept constant of diameter 60 mm while the tapered ratio of the basin was varied by varying bottom cone diameters in three steps: 60 mm, 100 mm and 150 mm as shown in Figure 4.1.

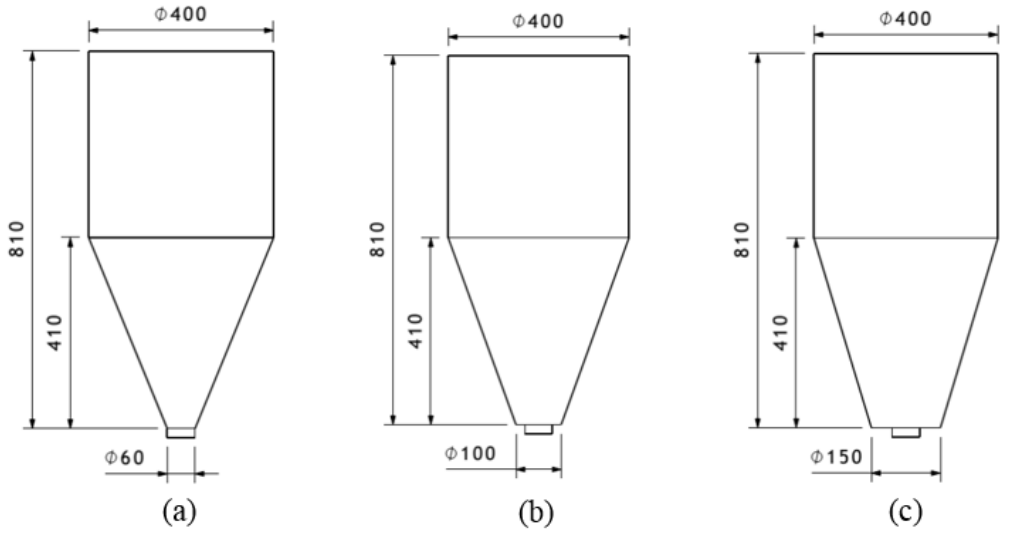

Figure 4.1 Basin with fixed outlet diameter and varying bottom cone diameter (a) 60 mm, (b) 100 mm & (c) 150 mm

4.1.1.1. Effect on Flow Pattern

The variations on air volume fraction rendering was observed in a longitudinal plane lying along the center of the inlet canal and were found as shown in Figure 4.2. It was observed that, a conical region of air were formed. This may be due to the presence of both fluid i.e., air and water in same domain and resembles to actual conditions of

vortex motion. However, with increasing bottom cone diameter, a slight reduction in the air region depression were observed. The air region formed throughout the conical basin started vanish with increasing bottom cone diameter.

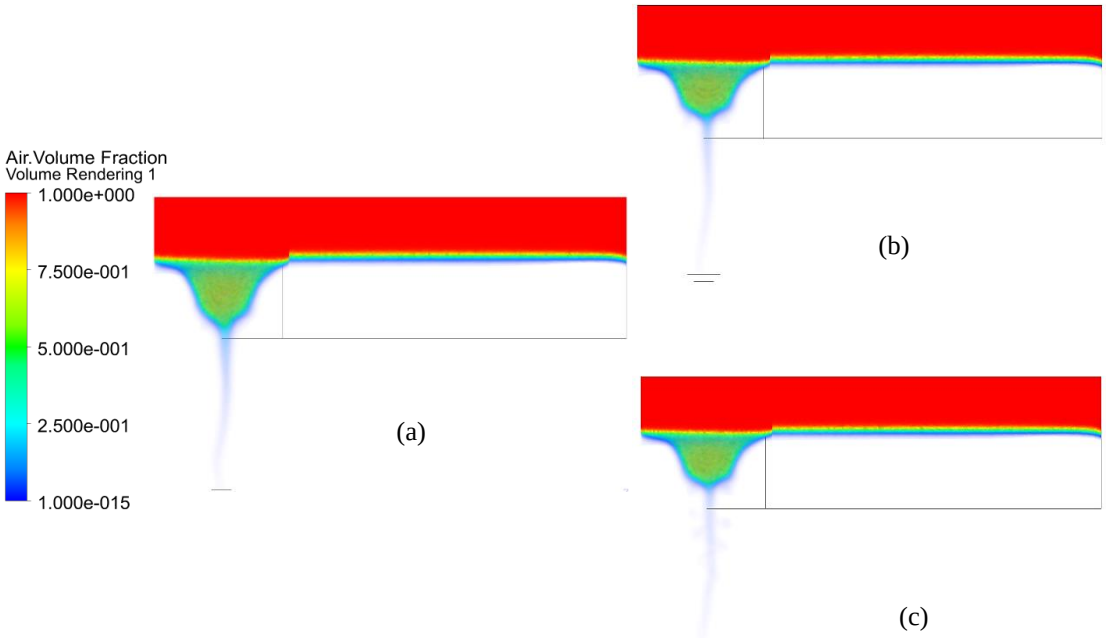

Figure 4.2 Variations in air volume fraction rendering due to (a) bottom cone diameter: 60 mm (b) bottom cone diameter: 100 mm & (c) bottom cone diameter: 150 mm

Similary, the water volume fractions were observed in a transverse plane that passes through the central axis of the conical basin and were as shown in Figure 4.3. The reduction in the depression of air region with increased bottom cone diameter resulted in increasing water region throughout the conical basin portion.

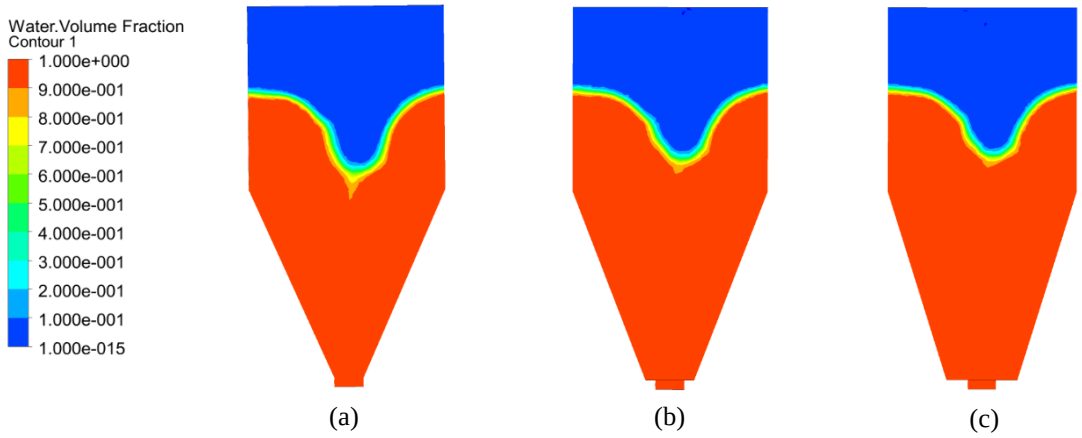

Figure 4.3 Variations in water volume fractions (a) bottom cone diameter: 60 mm (b) bottom cone diameter: 100 mm & (c) bottom cone diameter: 150 mm

4.1.1.2. Effect on Runner Profile

The runner profile for each varying bottom diameters were obtained as shown in Figure 4.4.

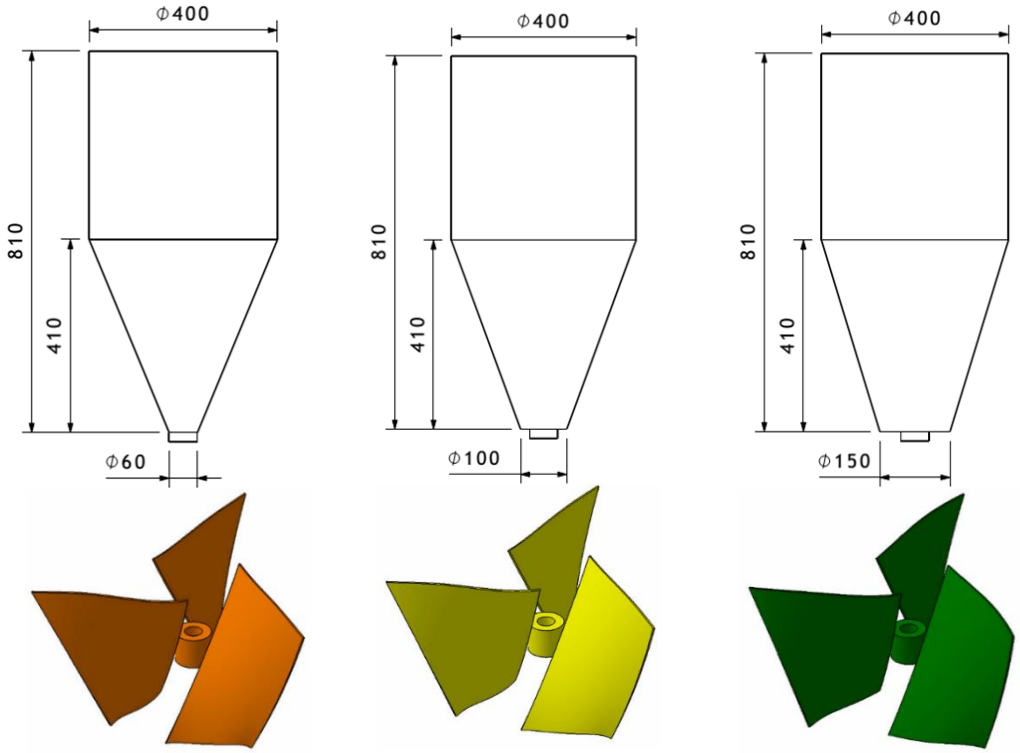

(a) (b) (c)

Figure 4.4 Runner profile with constant exit hole (dia. 60mm) and (a) bottom diameter: 60 mm (b) bottom diameter: 100 mm & (c) bottom diameter: 150 mm

As depicted in figure, not much variations on runner profile were observed for varying bottom cone diameters except for a little change in top edge of the runner. The top edge was observed to change from concave outward to concave inward.

4.1.2. Variation of Runner Profile with Changing Exit Hole

In this case, the tapered ratio of the basin were varied by varying diameters of the basin exit hole as 50 mm, 60 mm, 70 mm & 80 mm as shown in Figure 4.5.

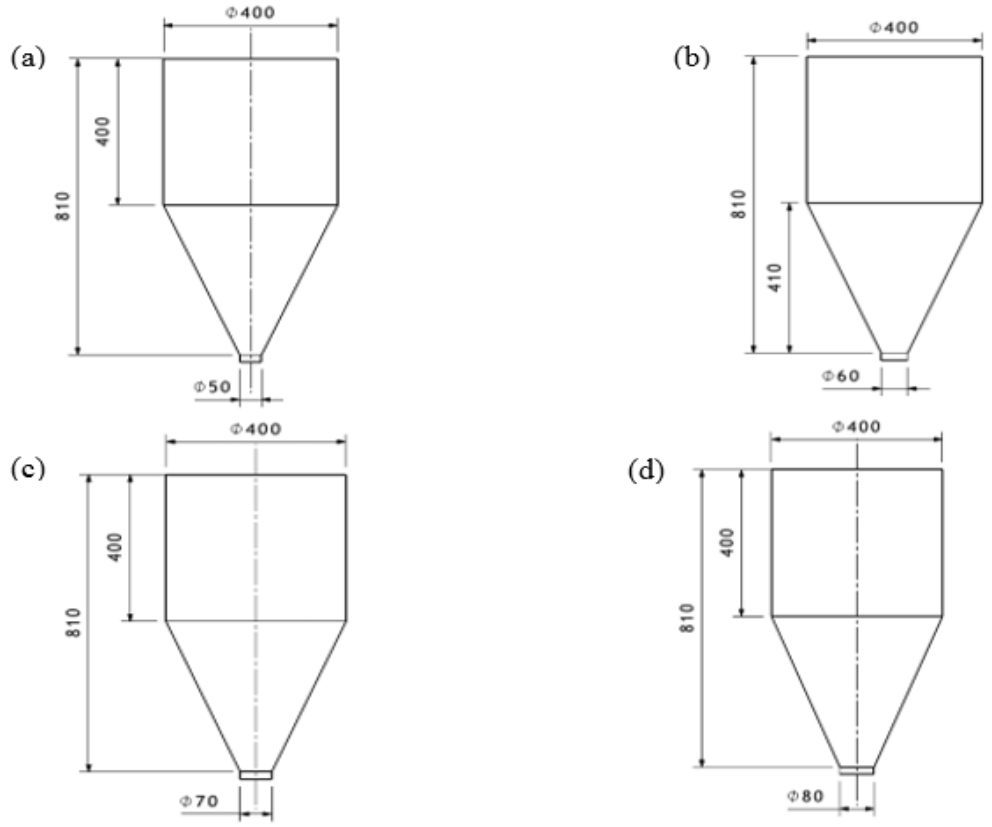

Figure 4.5 Basin with varying outlet diameter of (a) 50 mm, (b) 60 mm, (c) 70 mm & (d) 80 mm

4.1.2.1. Effect on Flow Pattern

The variations on air volume fraction rendering and water volume fraction contour were observed and were found as shown in Figure 4.6. As can be observed in the figure that increasing the outlet diameter of the basin resulted in the formation of dense conical region of air that extended upto the exit hole of the basin from its top surface.

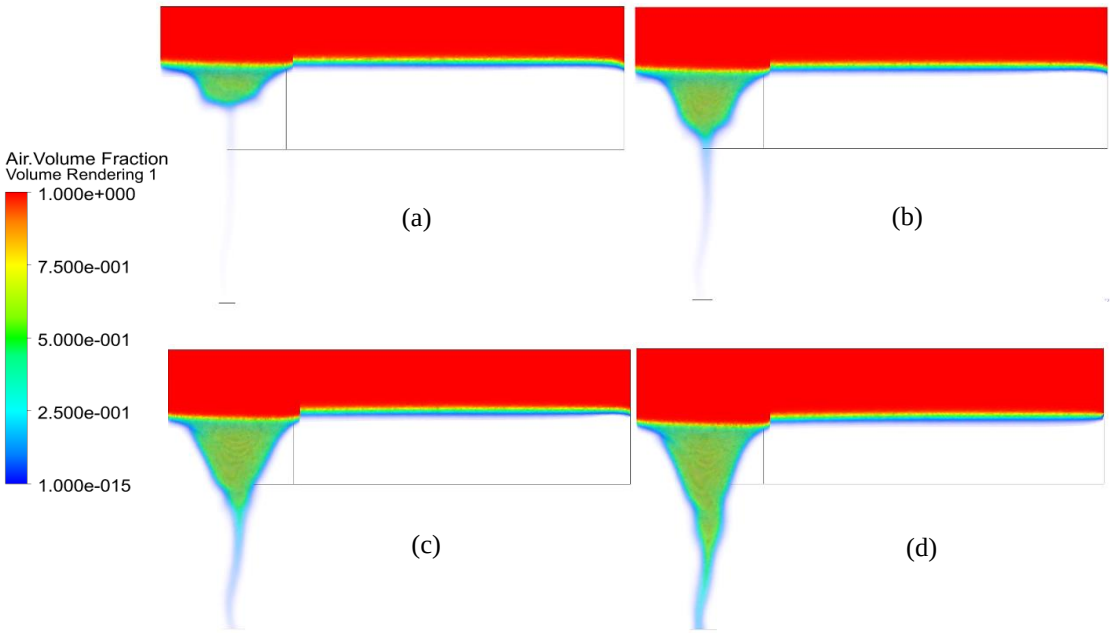

Figure 4.6 Variations in air volume fraction rendering at outlet diameter (a) 50 mm, (b) 60 mm, (c) 70 mm & (d) 80 mm

Also, the variation of water volume fractions were observed as shown in Figure 4.7.

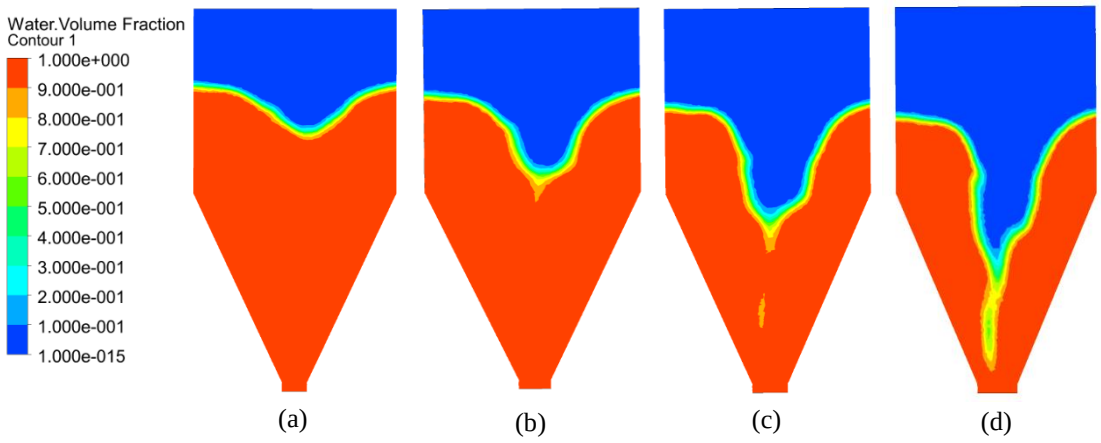

Figure 4.7 Variations in water volume fractions at outlet diameter (a) 50 mm, (b) 60 mm, (c) 70 mm & (d) 80 mm

As the exit hole diameter was increased, air region depression started to dominate water region throughout conical basin thereby reducing the water portion inside the basin. This may be be due to lower velocity of water through the inlet canal and resembles to pouring of water in the vessel.

4.1.2.2. Effect on Runner Profile

The runner profile for different exit hole diameter were obtained as shown in Figure 4.8. On increasing the diameter of outlet hole, the runner top edge was found to change from concave outward to concave inward. However, abrupt change was noticed on

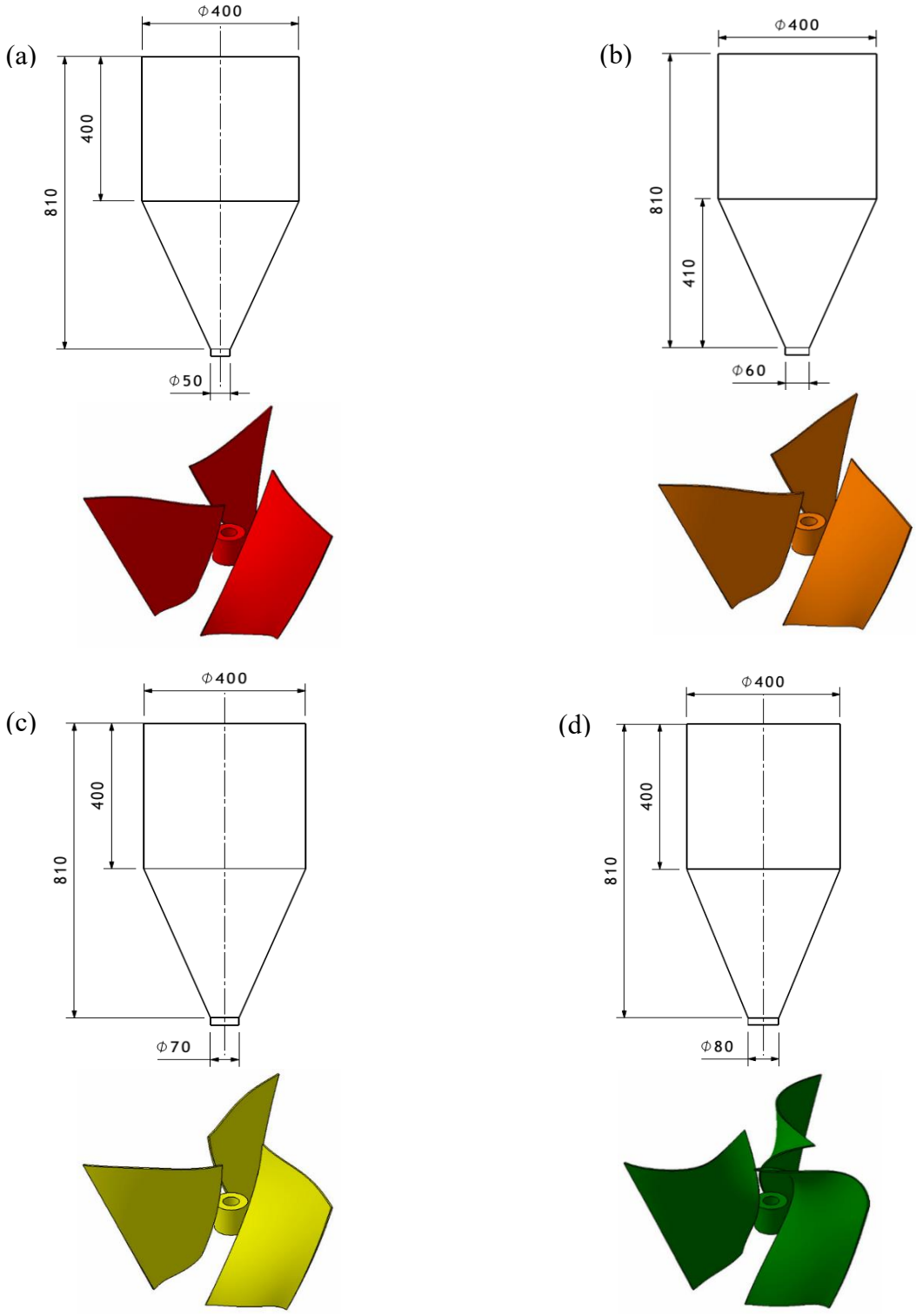

Figure 4.8 Runner profile outlet diameter (a) 50 mm, (b) 60 mm, (c) 70 mm & (d) 80 mm

runner top edge in Figure 4.8 (d). This may be due to the fact that, with increasing exit hole diameter, the air region started dominating the water region which can be observed in Figure 4.7 (a) - (d). The points considered near the hub region during design therefore lied on the air region instead of water region where the water velocity vectors had upward components thereby resulting the profile blocking the water going upwards perpendicularly.

4.2. Performance Evaluation of Reference Runner

For the performance evaluation of runner, a runner developed for reference basin was selected so that later on its results can be validated with the experimental data. The speed of the runner was changed from 55 rpm to 76 rpm and the corresponding torque value acting on the runner blades and power developed by the runner were determined as shown in Figure 4.9 and Figure 4.10 respectively.

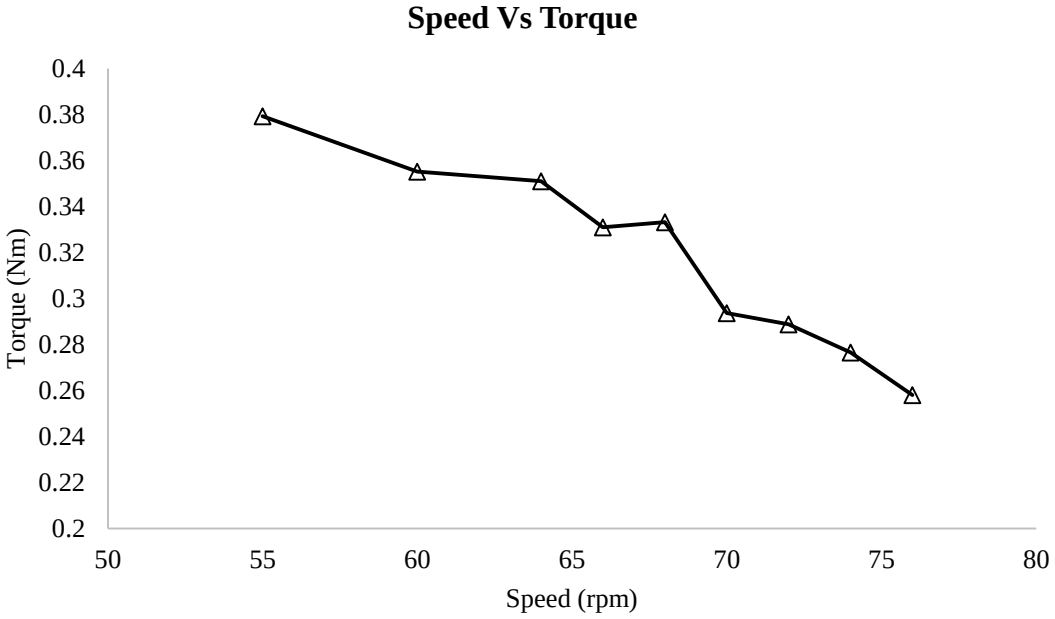

Figure 4.9 Variations of torque with speed of runner

As can be seen from the figure, the torque value increases with the reduction in speed of the runner.

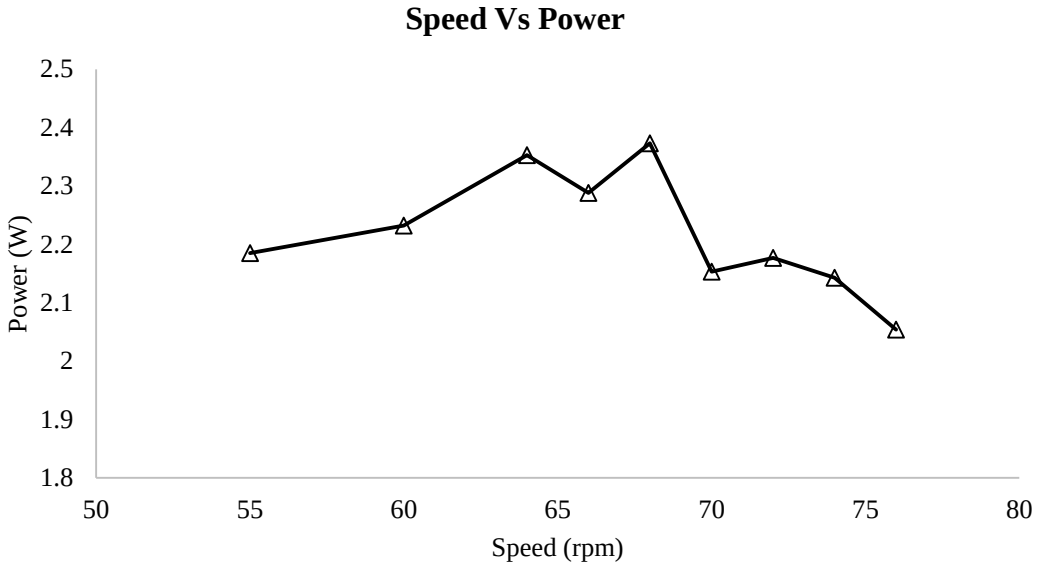

Figure 4.10 Variations of power developed with speed of runner

From the figure, it is found that maximum power of 2.373 watt is developed by runner when the speed of the runner was 68 rpm. Further increment and decrement in the speed shows the reduction in developed power.

For calculation of efficiency, the previous study by (Dhakal, et al., 2015; Sapkota, et al., 2016) has adopted the following formula and the same formula had been used for efficiency calculation in this study.

$$P_{in} = \rho g H Q \qquad \text{Equation 4.1}$$

Where,

ρ = Density of water taken ($1000\ kg/m^3$)

g = Acceleration due to gravity ($9.81\ m/s^2$)

H = Available head upto runner mean height ($0.305\ m$)

Q = Flow rate ($0.25 \times 0.2 \times 0.2 = 0.01 m^3/s$)

Using Equation 4.1, the input power was calculated to be 29.9205 watt. With the calculated input power, the efficiency of the reference runner was determined at different speed as shown in Figure 4.11.

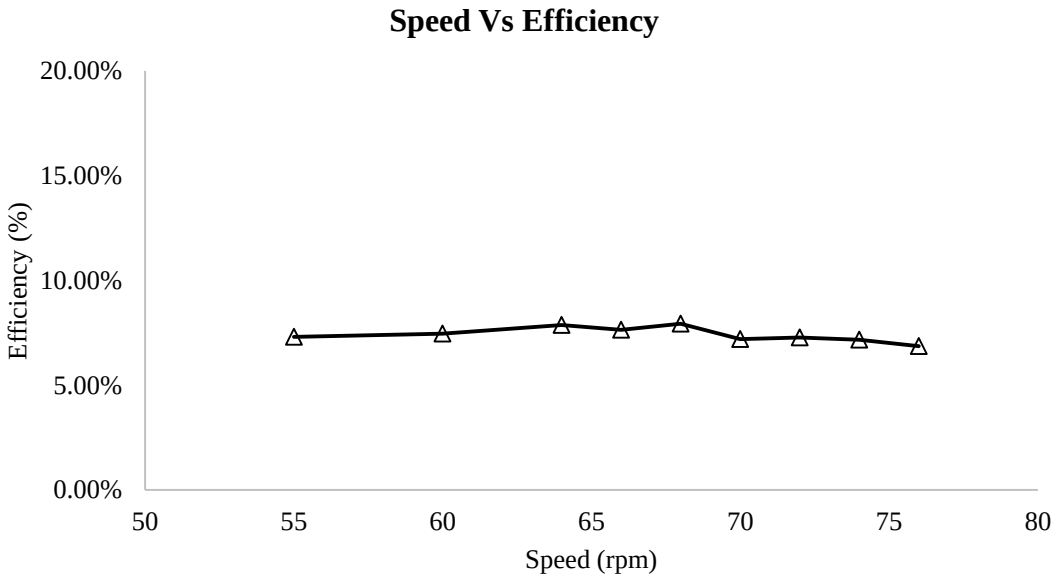

Figure 4.11 Efficiency of reference runner at different runner speed

The maximum efficiency was observed to be 7.93% when the runner speed is 68 rpm.

4.3. Performance Evaluation of Runner for Basin with Exit hole Diameter 50 mm

The performance evaluation of runner designed for basin with exit hole diameter 50mm was also carried out. For evaluation, the runner domain was rotated at different speed in the range 60 to 72 rpm and the corresponding torque developed in the runner blades were obtained from CFD analysis and the graph plotted between runner speed and torque developed is as shown in Figure 4.12.

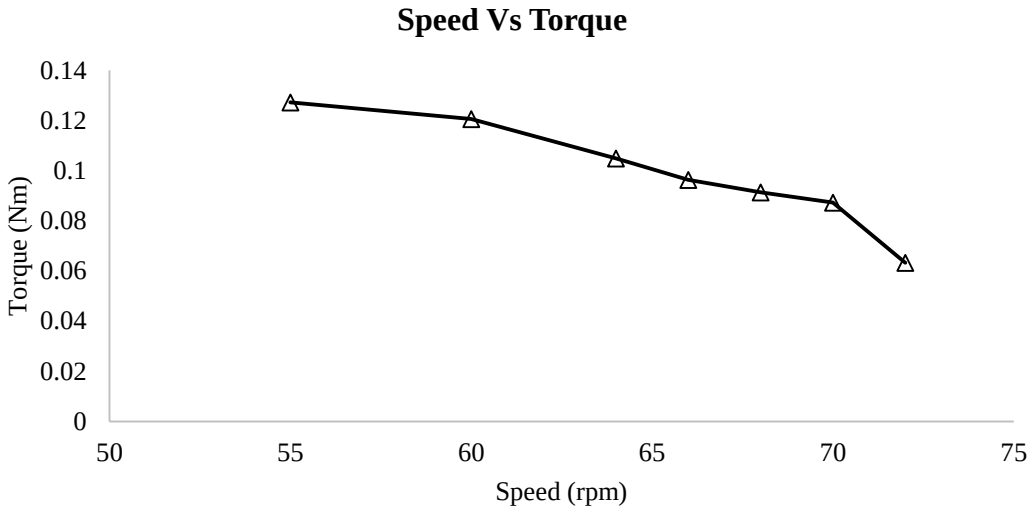

Figure 4.12 Variations of torque with speed of runner

The torque value obtained was about three to four times less than the torque value obtained for reference runner at same rpm. Corresponding power output by this runner at different rpm is as shown in Figure 4.13.

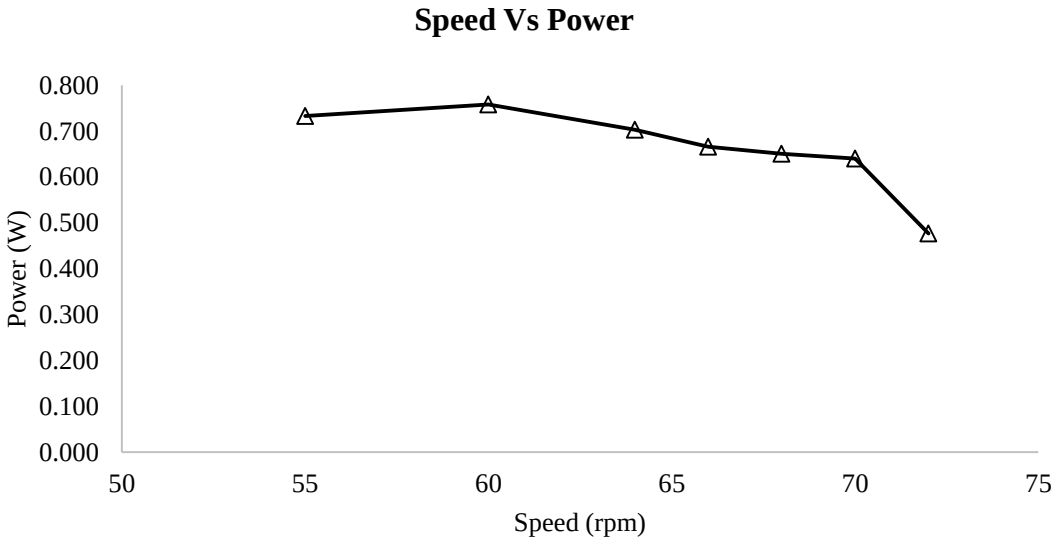

Figure 4.13 Variations of power developed with speed of runner

The maximum power developed by this runner was 0.758 watt at 60 rpm which is around three times less than that of power developed by reference runner. Also the maximum efficiency of this runner was found to be 2.53% as shown in Figure 4.14.

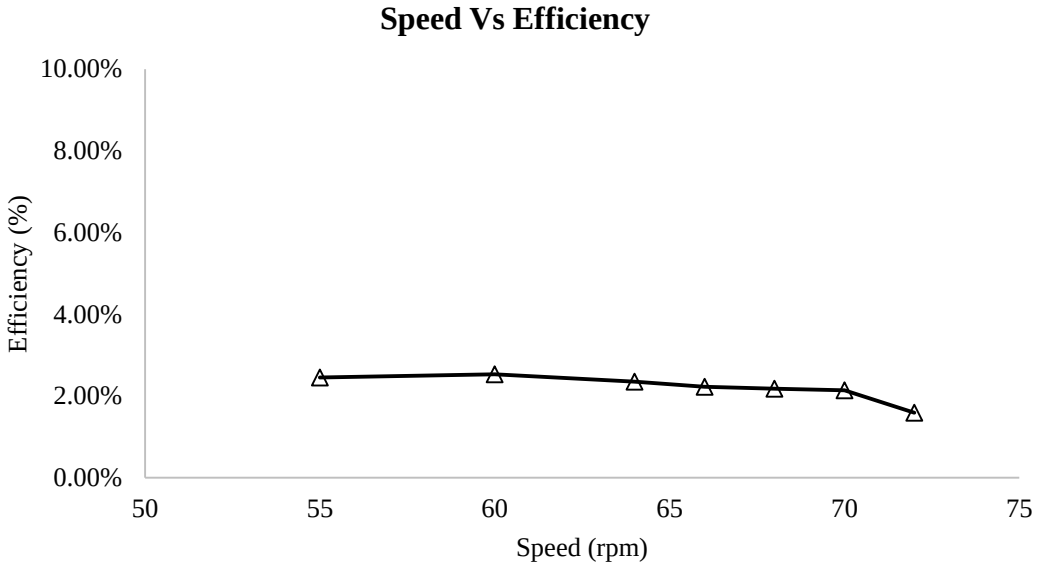

Figure 4.14 Efficiency at different runner speed

All these results showed that, the efficiency of the designed runner was reduced for smaller value of exit hole.

4.4. Comparative Analysis of the Computational and Experimental Results

The experimental analysis of the runner designed for reference basin was carried out. The runner speed was varied from 53 rpm to 93 rpm by adjusting load on one of two spring balances used in the experiment and the corresponding torque developed were calculated from the data observed from experiment. The observed experimental torque values were then plotted along with the computational torque values against runner speed as shown in Figure 4.15.

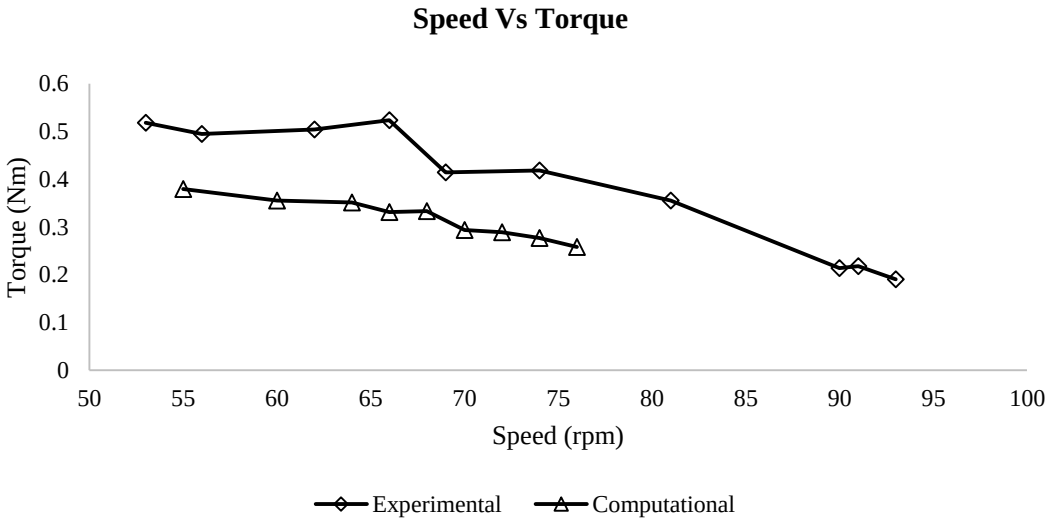

Figure 4.15 Comparison of torque obtained from experimental and computational analysis

The torque values obtained from experiment were found to be greater than that obtained from computational analysis. The higher torque values obtained for a given speed from

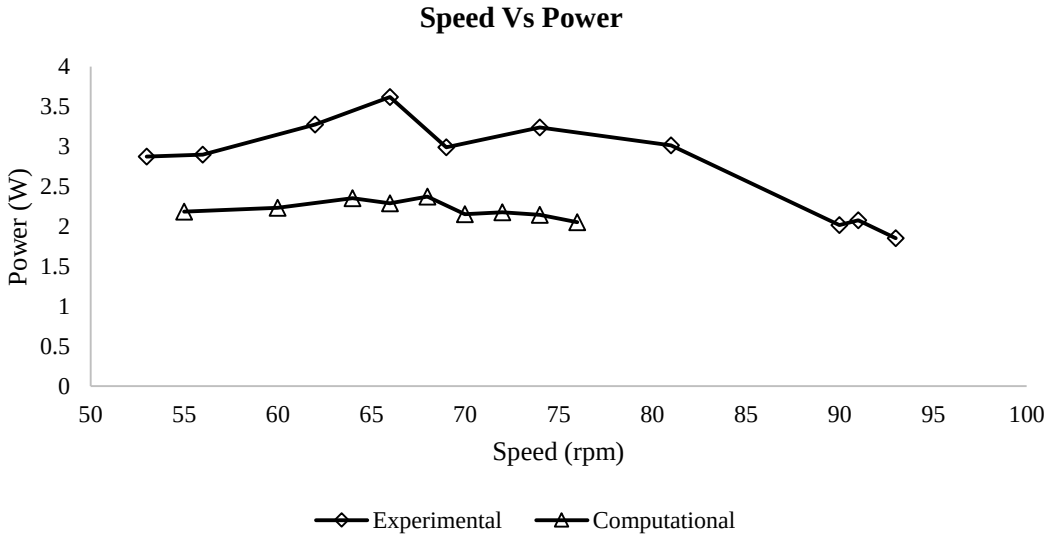

Figure 4.16 Comparison of output power obtained from experimental and computational analysis

experiment therefore resulted in higher braking power than obtained from experiment as shown in Figure 4.16.

The maximum output power obtained experimentally was 3.6206 watt at 66 rpm while the value was 2.373 watt from computational analysis at 68 rpm. The efficiencies of the runner was then determined experimentally and plotted with that of computational efficiencies against the runner speed and was obtained as shown in Figure 4.17.

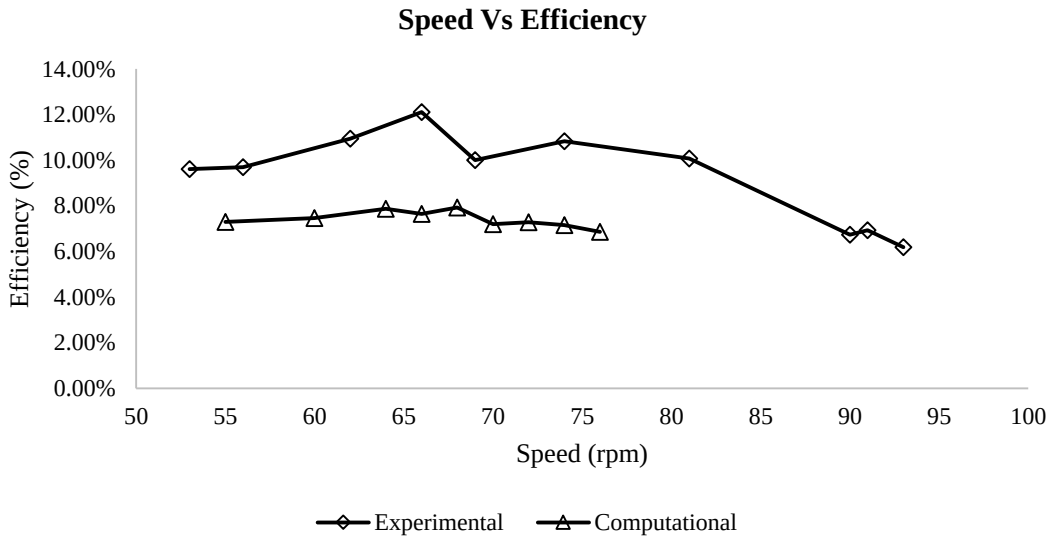

Figure 4.17 Comparison of efficiency obtained from experimental and computational analysis

The maximum efficiency obtained from experiment was 12.10% at 66 rpm while the computational efficiency was found to be 7.65% at 66 rpm. However, computational analysis revealed the maximum efficiency of 7.93% at 68 rpm. The maximum experimental efficiency value was found to be greater by 4.45% than obtained from computational analysis at 66 rpm. Considering the best efficiency point, the maximum experimental efficiency was greater by 4.17% than maximum efficiency obtained from computational analysis.

The variations between experimental and computational results may be due to the following possible causes:

i. Deviations in the actual and casted profile of runner

   Although the 3D printed blade profile was provided to the manufacturer for casting purpose, some variations may have been occured during casting process due to conventional method adopted by manufacturer while casting. The

variations on the blade profile can be observed by placing the actual 3D printed profile over the casted blade profile. However, not much significant variations was observed in the casted blade.

ii. Deviations in the orientation of blade during welding

It was difficult obtaining the slots in hub from casting process for placing blade as available in 3D printed hub. Hence, the hub was casted as a solid shaft which was later machined to appropriate dimension but still no slots were created. So, welding of the blade in the machined hub following actual vertical orientation was quite difficult and may have varied than it had to be. However, effort has been applied to weld the blade in vertical orientation as that obtained from 3D printing.

iii. Variations in the flow rate during experimental analysis

The water through the canal of test rig was continuously overflowing from top surface and may have reduced the flow rate than actual flow while striking the runner. Though the overflowing was compensated by continuous supply of water to the test rig chamber ensuring the required water level in the notch but this was not going to solve the flow rate striking the runner.

The possible causes explained in (i) and (ii) may be the accidental indication that there is a need for corrections in blade profile and vertical orientation while attaching blades to hub, thereby increasing the efficiency of the runner.

CHAPTER-FIVE: CONCLUSIONS AND RECOMMENDATIONS

5.1. Conclusions

The major findings of thesis work can be summarized as below

i. Conical basin (reference basin) with inlet height 400 mm and canal length 1200 mm was used as a reference basin for generating blade profile and CFD analysis was carried out using multiphase approach.

ii. For a given flow rate, head and runner placement position, runner profile can be generated.

iii. The maximum efficiency of designed runner was found 7.93 % at 68 rpm from computational analysis while experimentally maximum efficiency was found to be 12.10 % at 66 rpm. However, comparison at the same runner speed of 66 rpm, the experimental maximum efficiency was found to be higher by 4.45% than computational efficiency 7.65%.

5.2. Recommendations

The following recommendations can be suggested for further study

i. Number of points initially considered for designing of runner can be increased for obtaining more accurate blade profile.

ii. Appropriate corrections can be applied on the obtained final points for generating blade profile so as to ensure that the flow strikes the runner blade perpendicularly at every considered points.

iii. Blade numbers can be varied (in this study limited to three) and comparative study on runner efficiency can be carried out.

iv. The comparative study on efficiency can be carried out by generating blade for different basin structure.

v. The computational studies on performance of the runner can be carried out using different turbulence model.

REFERENCES

Abbasi, T. & Abbasi, S. N., 2011. Small hydro and the environmental implications of its extensive utilization. *Renewable and Sustainable Energy Reviews,* Volume 15, pp. 2134-2143.

Anderson, J. J. D., 2001. *Fundamental of Aerodynamics.* 3rd ed. New York, America: Mc Graw Hill.

Bakker, A., 2008. *Microsoft PowerPoint - 01-intro.ppt.* [Online] Available at: http://www.bakker.org/dartmouth06/engs150/01-intro.pdf [Accessed 14 December 2018].

Banerjee, S. G., Singh, A. & Samad, H., 2011. *Power and People: The Benefits of Renewable Energy in Nepal,* Washington, DC: The World Bank.

Dhakal, R., Chaulagain, R. K., Bajracharya, T. R. & Shrestha, S., 2015. *Economic feasibility study of gravitational water vortex power plant for the rural electrification of low head region of Nepal and its comparative study with other low head power plant.* Kathmandu, Nepal, Journal of 11th International conference "ASIAN community knowledge networks for the economy, society, culture and environmental stability, pp. 127-135.

Dhakal, R. et al., 2016. *Computational and experimental investigation of a runner; gravitational vortex power plant.* s.l.:s.n.

Dhakal, S. et al., 2014. *Development and Testing of Runner and Conical Basin Gravitational Water Vortex Power Plant.* Pulchowk, Lalitpur, Center for Energy Studies (CES), Institute of Engineering, Tribhuwan University, Nepal.

Dhakal, S. et al., 2015. Comparison of cylindrical and conical basins with optimum position of runner: Gravitational water vortex power plant. *Renewable and Sustainable Energy Reviews,* Volume 48, pp. 662-669.

Donaldson, C. d., 1960. *Examination of the solutions of the Navier-Stokes equations for a class of three-dimensional vortices.* s.l.:Princeton, N.J.: Aeronautical Research Associates of Princeton.

Gheroghe, M. M., Tudor, S. & Abdelkrim, A., 2013. Study of Micro Hydropower Plant Operating in Gravitational Vortex Flow Mode. *Applied Mechanics and Materials,* Volume 371, pp. 601-605.

Jost, D., Skerlavaj, A. & Lipej, A., 2014. Improvement of Efficiency Prediction for a Kaplan Turbine with Advanced Turbulence Models. *Journal of Mechanical Engineering*, 60(2), pp. 124-134.

Kueh, T. C., beh, S. L., rilling, D. & Ooi, Y., 2014. Numerical Analysis of Water Vortex Formation for Water Vortex Power Plant. *International Journal of Innovation, Management and Technology*, 5(2), pp. 111-115.

Lamb, H., 1993. *Hydrodynamics.* 4th ed. s.l.:Cambridge University Press.

Lepisto, C., 2007. *Gravitational Vortex Power Plant is Safe for Fish | TreeHugger.* [Online]
Available at: https://www.treehugger.com/renewable-energy/gravitational-vortex-power-plant-is-safe-for-fish.html
[Accessed 08 November 2018].

Lewellen, W., 1962. A solution for three-dimensional vortex flows with strong circulation. *Journal of Fluid Mechanics*, 14(3), pp. 420-432.

MARIAN, G.-M.et al., 2012. THE CONCEPT AND THEORETICAL STUDY OF MICRO HYDROPOWER PLANT WITH GRAVITATIONAL VORTEX AND TURBINE WITH RAPIDITY STEPS. *World Energy System Conference*, Issue 3, pp. 219-226.

Marius-Gheorghe, M., Tudor, S. & Abdelkrim, A., 2013. Study of Micro Hydropower Plant Operating in Gravitational Vortex Flow Mode. *Applied Mechanics and Materials,* Volume 371, pp. 601-605.

Mulligan, S. & Casserly, J., 2010. *The Hydraulic Design and Optimization of a Free Water Vortex for the Purpose of Power Extraction*, s.l.: Department of Civil Engineering, Institute of Technology Sligo.

Mulligan, S. & Hull, P., 2010. *Design and Optimization of water vortex hydropower plant,* Sligeach: Department of Civil Engineering and Construction, IT Silgo.

Power, C., McNabola, A. & Coghlan, P., 2016. A Parametric Experimental Investigation of the Operating Conditions of Gravitational Vortex Hydropower (GVHP). *Journal of Clean Energy Technologies*, 4(2), pp. 112-119.

Pritchard, P. J., 2010. *Fox and McDonald's Introduction to Fluid Mechanics.* New Jersey: JOHN WILEY & SONS, INC..

Rahman, M. M. et al., 2016. Experimental Study the Effects of Water Pressure and Turbine Blade Lengths & Numbers on the Model Free Vortex Power Generation System. *International Journal of Current Trends in Engineering & Research,* 2(9), pp. 13-17.

Rahman, M. M., Tan, J. H., Fadzlita, M. T. & Wan Khairul Muzammil, A. R., 2017. A Review on the Development of Gravitational Water Vortex Power Plant as Alternative Renewable Energy Resources. *IOP Conference Series: Materials Science and Engineering*, Volume 217, pp. 1-9.

Sapkota, A., Gautam, A., Dhakal, J. & Neupane, S., 2016. *Design Study of Runner for Gravitational Water Vortex Power Plant with Conical Basin,* Lalitpur: Department of Mechanical Engineering.

Shtern, V., Borissov, A. & Hussain, F., 1997. Vortex sinks with axial flow: Solution and applications. *Physics of Fluids,* 9(10), pp. 2941-2959.

Singh, P. & Nestmann, F., 2009. Experimental Optimization of a free vortex propeller runner for micro hdyro application. *Experimental Thermal and Fluid Science,* Volume 33, pp. 991-1002.

Tu, J., Yeoh, G.-H. & Liu, C., 2018. *Computational Fluid Dynamics- A Practical Approach.* 3rd ed. 50 Hampshire Street, 5th Floor, Cambridge, MA 02139, United States: Butterworth-Heinemann.

Wanchat, S. & Suntivarakorn, R., 2011. Preliminary design of a vortex pool for. *Journal of Computational and Theoretical Nanoscience,* 13(1).

Wanchat, S. et al., 2013. A Parametric Study of a Gravitation Vortex Power Plant. *Advanced Materials Research,* Volume 805-806, pp. 811-817.

Wichian, P. & Suntivarakorn, R., 2016. The Effects of Turbine Baffle Plates on the Efficiency of Water Free Vortex Turbines. *Energy Procedia,* Volume 100, pp. 198-2020.

WU, C., WANGa, B. & CHEN, M. D. Y., 2012. Three-dimensional Numerical Simulation of Vertical Vortex at Hydraulic Intake. *Elsevier*, Volume 28, pp. 55-60.

Zotloeterer.com, 2011. *ZOTLÖTERER-TURBINE.* [Online] Available at: http://www.zotloeterer.com/welcome/gravitation-water-vortex-power-plants/zotloeterer-turbine/
[Accessed 24 December 2016].

Zotlöterer, 2016. *Wayback Machine.* [Online] Available at: https://web.archive.org/web/20160303171227/http://www.pureenergysystems.com/NEC/conferences/2008/EnvironmentalHallofFame--Chicago/displays/Zotloterer.pdf
[Accessed 24 August 2018].

Accepted Paper Detail:

Regmi, N., Dura, H., & Shakya, S. R. (2019). Design and Analysis of Gravitational Water Vortex Basin and Runner. *IOE Graduate Conference, 2019.*

ANNEX-1: INDEPENDENCE ANALYSIS DATA

Table 5.1 Mesh Independence Analysis Data

S.N.	Elements Number	Torque (Nm)
1	112,954	0.0713513
2	213,576	0.11258
3	310,667	0.138181
4	405,804	0.153172
5	603,018	0.162332
6	813,080	0.168306
7	1,039,630	0.173774

Table 5.2 Air Domain Height Independence Analysis Data

S.N.	Air Domain Height (mm)	Torque (Nm)
1	0.00	0.166506
2	100.00	0.165950
3	200.00	0.162072
4	400.00	0.160173

Table 5.3 Canal Length Independence Analysis Data

S.N.	Canal Length (mm)	Torque (Nm)
1	880.00	0.168306
2	1200.00	0.169072
3	1600.00	0.170831
4	2000.00	0.173089
5	3000.00	0.174173

ANNEX-2: COMPUTATIONAL RESULTS

Table 5.4 Computational Results (Torque, Power & Efficiency) for Reference Runner

Speed (rpm)	Torque (Nm)	Power (W)	Efficiency (%)
55	0.379329	2.185	7.30%
60	0.35523	2.232	7.46%
64	0.351064	2.353	7.86%
66	0.331021	2.288	7.65%
68	0.333238	2.373	7.93%
70	0.293699	2.153	7.20%
72	0.288706	2.177	7.28%
74	0.276511	2.143	7.16%
76	0.25805	2.054	6.86%

Table 5.5 Computational Results (Torque, Power & Efficiency) for Runner Designed for Basin with Exit Hole Diameter 50 mm

Speed (rpm)	Torque (Nm)	Power (W)	Efficiency (%)
55	0.127217	0.733	2.45%
60	0.120571	0.758	2.53%
64	0.104855	0.703	2.35%
66	0.096323	0.666	2.23%
68	0.091354	0.651	2.18%
70	0.087247	0.640	2.14%
72	0.063275	0.477	1.59%

ANNEX-3: COST SUMMARY

Table 5.6 Cost Involved in Fabrication and Experiment Works

S.N.	Particulars		Quantity	Unit Cost (NRs.)	Total Cost (NRs.)	Remarks
Fabrication Cost						
1	3D Print (Hub & Blades)		-	-	7,500.00	Zener Technologies, Kupondole, Kathmandu
2	Casting	Blades (3 Nos.)	4.01 kg	1300 per kg	5,213.00	Tuladhar Metal Works, Bijeshwori, Kathmandu
		Hub	6.3 kg	1150 per kg	7,245.00	
3	Lathe Operations (Turning, Facing, boring)		2 hrs.	600 per hr.	1,200.00	Shrestha Lathe Milling Workshop, Sinamangal, Kathmandu
4	Gas Welding		-	-	7,000.00	Shumsher and Chhotu Auto Workshop, Bhotebahal, Kathmandu
Experiment Cost						
1	Hanging Weighing Scale		2 Set	700 per set	1,400.00	
2	Jute rope		2 Set	10 per set	20.00	
3	Bolt		1 Nos.	10 per No.	10.00	
Gross Total Cost (NRs.)					**29,558.00**	

ANNEX-4 EXPERIMENTAL DATA

Table 5.7 Experimental Data for Reference Runner

S.N.	Flow rate, Q (m^3/s)	Runner top edge position from top water surface level (m)	Drum radius, R_D (m)	Weight attached, W (kg)	Spring balance reading, S (kg)	Speed, N (rpm)	Braking torque, T_B (Nm)	Brake power, P_B (watt)	Power available, P_I (watt)	Efficiency (%)
1	0.010	0.200	0.040	2.440	1.120	53	0.5180	2.8748	29.9205	9.61%
2	0.010	0.200	0.040	2.370	1.110	56	0.4944	2.8995	29.9205	9.69%
3	0.010	0.200	0.040	2.325	1.040	62	0.5042	3.2738	29.9205	10.94%
4	0.010	0.200	0.040	2.285	0.950	66	0.5239	3.6206	29.9205	12.10%
5	0.010	0.200	0.040	2.075	1.020	69	0.4140	2.9913	29.9205	10.00%
6	0.010	0.200	0.040	1.885	0.820	74	0.4179	3.2385	29.9205	10.82%
7	0.010	0.200	0.040	1.595	0.690	81	0.3551	3.0123	29.9205	10.07%
8	0.010	0.200	0.040	0.915	0.370	90	0.2139	2.0156	29.9205	6.74%
9	0.010	0.200	0.040	0.835	0.280	91	0.2178	2.0754	29.9205	6.94%
10	0.010	0.200	0.040	0.815	0.330	93	0.1903	1.8535	29.9205	6.19%